UNCLASSIFIED

(2)

SECURITY CLA

AD-A238 857

...TION PAGE

Form Approved
OMB No. 0704-0188

1a. REPORT S
Unclas

1b. RESTRICTIVE MARKINGS

2a. SECURITY

3. DISTRIBUTION/AVAILABILITY OF REPORT
Approved for public release; distribution unlimited

2b. DECLASSIFICATION/DOWNGRADING SCHEDULE

4. PERFORMING ORGANIZATION REPORT NUMBER(S)
VPI-AOE-179

5. MONITORING ORGANIZATION REPORT NUMBER(S)
AFOSR-TR- 91 0646

6a. NAME OF PERFORMING ORGANIZATION
Aerospace and Ocean Engineering Dept.

6b. OFFICE SYMBOL (If applicable)

7a. NAME OF MONITORING ORGANIZATION
AFOSR/NA
Bolling AFB DC 20332-6448

6c. ADDRESS (City, State, and ZIP Code)
Virginia Polytechnic Institute and State University
Blacksburg, VA 24061

7b. ADDRESS (City, State, and ZIP Code)
AFOSR/NA
Bolling AFB DC 20332-6448

8a. NAME OF FUNDING/SPONSORING ORGANIZATION
Air Force Office of Scientific Research

8b. OFFICE SYMBOL (If applicable)
NA

9. PROCUREMENT INSTRUMENT IDENTIFICATION NUMBER
F49620-88-C-0043P00005

8c. ADDRESS (City, State, and ZIP Code)
AFOSR/NA Bldg. 410
Bolling AFB, Washington, DC 20332-6448

10. SOURCE OF FUNDING NUMBERS

PROGRAM ELEMENT NO.	PROJECT NO.	TASK NO.	WORK UNIT ACCESSION NO.
61102F	2307	A3	

11. TITLE (Include Security Classification)
Three-Dimensional Rapidly Scanning Laser Doppler Velocimeter with Low SNR Signal Processing

12. PERSONAL AUTHOR(S)
Kevin A. Shinpaugh and Roger L. Simpson

13a. TYPE OF REPORT	13b. TIME COVERED	14. DATE OF REPORT (Year, Month, Day)	15. PAGE COUNT
Final	FROM 2/1/88 TO 11/30/90	1990 November 30	129

16. SUPPLEMENTARY NOTATION

17. COSATI CODES			18. SUBJECT TERMS (Continue on reverse if necessary and identify by block number)
FIELD	GROUP	SUB-GROUP	Laser anemometry or velocimetry Signal Processing
14	02		
20	04		

19. ABSTRACT (Continue on reverse if necessary and identify by block number)

A rapidly scanning directionally sensitive three-velocity-component laser Doppler velocimeter (RSLDV) has been designed. It permits rapid scans through three-dimensional flows to obtain space-time velocity information and almost "instantaneous" velocity profiles vital to understanding such flows.

A flexible optical system allows for easy variation of the fringe spacing as well as the location and size of the measurement volume. Several optical techniques to maintain coincidence between the horizontal, U and W, and vertical, V, probe volumes were investigated. A lens, used like a prism, and two plane mirrors for the out of plane scanning laser beam maintains good coincidence between the probe volumes, while maintaining some flexibility. Moving fringe patterns in the horizontal and vertical planes are produced by a dual water Bragg cell. The Doppler frequency is independent of the positon of the receiving optics, and only one photomultiplier tube (PMT) is needed to receive the signals for all three velocity components.

(see back)

20. DISTRIBUTION/AVAILABILITY OF ABSTRACT
☒ UNCLASSIFIED/UNLIMITED ☐ SAME AS RPT ☐ DTIC USERS

21. ABSTRACT SECURITY CLASSIFICATION
NONE

22a. NAME OF RESPONSIBLE INDIVIDUAL
Daniel Fant, Maj, USAF

22b. TELEPHONE (Include Area Code)
202-767-0471

22c. OFFICE SYMBOL
AFOSR/NA

DD Form 1473, JUN 86

Previous editions are obsolete.

SECURITY CLASSIFICATION OF THIS PAGE
UNCLASSIFIED

19. Abstract

A data acquisition, control and processing system has also been designed for use with the RSLDV. The PMT signal and location of the measurement volume are recorded simultaneously by two transient recorders. The system provides storage for up to 1.25 gigabytes (6 secs.) of LDV data, with permanent storage onto optical disk. A 20 MFLOP array processor provides for fast computation of velocity information.

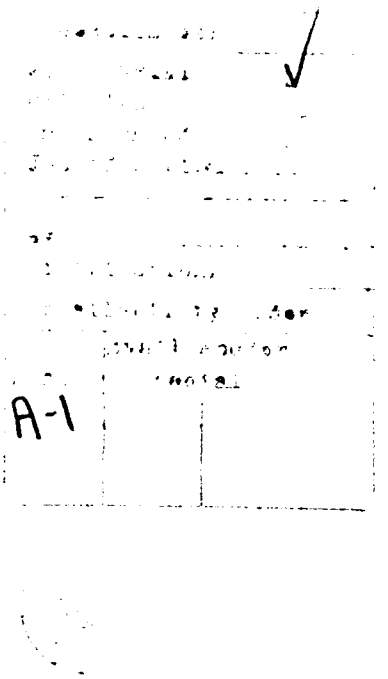

Table of Contents

List of Tables

List of Illustrations

List of Symbols

d .....x location of prism apex

d_1 .....x location of mirror M13

d_2 .....x location of mirror M14

DFT.....discrete Fourier transform

f.....focal length of lens

f.....frequency

f_d.....Doppler frequency

F.....optimization parameter

FFT.....fast Fourier transform

I.....laser beam intensity

j.....imaginary constant, $\sqrt{-1}$

L.....location of measurement volume measured from final lens

L_p.....length of vertical probe volume

m .....magnification factor

n .....index of refraction

PMT.....photomultiplier tube

RMS .....root mean square

R.....radius of curvature for concave mirror or lens surface

s.....object distance from lens

s'' .....image distance from lens

SNR.....signal to noise ratio

T.....temporal sampling interval

U .....velocity component in the x direction

V .....velocity component in the y direction

V_s.....scan velocity of measurement volume

W .....velocity component in the z direction

x_p .....location of measurement volume measured from scanning mirror

x_0 .....path length difference between central beam and two side beams without mirrors M6 and M7

x_{M1} .....x location of beam C on mirror M13

x_{M2}.....x location of beam C on mirror M14

y .....scan height of measement volume

y_{M1} .....y location of beam C on mirror M13

y_{M2} .....y location of beam C on mirror M14

Z_R.....Rayleigh range of input beam, $\frac{\pi\omega_0^2}{\lambda}$

Z''_R .....Rayleigh range of output beam

Greek symbols

α .....angle of intersection between beams A and B or$D$

δ .....change in angle of beam C for concave mirror or prism

ε.....wedge angle for prism

η .....fringe visiblity

θ .....scan angle

θ_0.....angle between beams A and$C$ at scanning mirror

θ_1 .....angle of inclination of mirror M13

θ_2.....angle of inclination of mirror M14

θ_r .....angle of inclination of output beam C from last optics

λ .....wavelength of laser light

λ_{AB} .....fringe spacing for interfernce pattern between laser beams A and B

ξ .....angle of intersection between beams C and B or D

ϕ.....angle of intersection between beams $A$and$B$ forming the vertical probe volume

ω_0 .....input beam waist

ω''_0.....output beam waist

1.0 Introduction

The Laser Doppler Velocimeter (LDV) has been a valuable tool for experimental investigation in fluid mechanics. The obvious advantage of LDV is its high frequency response and its ability to measure direction and magnitude of the velocity accurately and non-intrusively under conditions where other instruments provide questionable results or cannot be used at all.

Although commercial pointwise LDV systems are available, further instrument development is needed. In order to obtain more detailed features in certain complicated flows, such as turbulent separated flows, "instantaneous" velocity profiles should be obtained. Therefore scanning LDV systems are needed because they yield nearly instantaneous velocity profiles and, concurrently, reduce the data acquisition time of velocity information in at least one direction. Furthermore, three-dimensional measurements should be made so that important space-time flow-structural information can be obtained.

This work is concerned with the development of a three-component rapidly scanning laser Doppler velocimeter and the associated data acquisition.

1.1 Background

Laser Doppler velocimetry (LDV) is an optical technique for measuring the local, instantaneous velocity of a flow. The basic principle of LDV is to split a laser beam into two equal intensity beams which are made to intersect at the measurement volume. The intersecting beams form stationary interference fringe patterns inside the measurement volume formed by the crossing beams.

The fringe pattern is made of light and dark regions and if the laser beams cross at their waists, parallel fringes will be formed with equal fringe spacing. The spacing of the fringes, λ_{AB}, is given by

$$\lambda_{AB} = \frac{\lambda}{2 \sin \varphi}$$

where φ is the half angle between the intersecting pair of beams and λ is the wavelength of the laser light.

In order to measure the velocity of the flow, tracer particles must be present in the fluid. These particles can be naturally occurring or artificially induced into the fluid but should be of appropriate size, density and shape so that the particles follow the flow. When a particle passes through the measuring

volume it scatters light that can be detected by a photodetector. The Doppler frequency of the scattered light is directly proportional to the particle velocity which is given by

$$f_d = \frac{2|U|}{\lambda} \sin \varphi$$

where $|U|$ is the magnitude of the instantaneous velocity component perpendicular to the optical axis.

For more information on the principles and practices of LDV see Durst, Melling, and Whitelaw (1981).

1.2 Previous Work: Scanning LDV

A brief description of a few scanning LDV systems developed and used so far, is given by Antoine (1985) and Simpson (1989). Bendick (1971) described an on-axis scanning LDV that used a translational oscillating mirror. This system was used for instantaneous velocity measurements in steady and pulsating water flow in a glass tube of 6 mm I. D. The operation of this design is limited to scan speeds of 0.4 m/s due to the inertia of the moving optics.

A two-color dual-beam backscatter LDV system accomplishing a scan by translating a lens in the direction of the optical axis was reported by Grant and Orloff (1973). Scan rates were limited to 1.5 m/s because of inertial

considerations. More information concerning the application of this design is given by Orloff and Biggers (1974) and Orloff, *et al.* (1975).

A backscatter scanning system was reported by Rhodes (1976). It is able to scan a distance of 30 cm at a frequency of 30 Hz, and measure velocities at 16 discrete positions using a large rotating wheel containing 16 ports. For more information concerning this design, see Gartrell and Jordan (1977) and Meyers (1979).

An optical system capable of measuring true instantaneous velocity profiles was reported by Nakatani, *et al.* (1978). Instead of using a moving scanning device, it employed a cylindrical lens to form a vertical measurement volume along a straight line. The design is relatively impractical and expensive because a series of optical fibers connected to photodetectors is needed to collect data over a large scan range with good resolution.

The design of Durst, Lehmann, and Tropea (1981) used a relatively large rotationally oscillating mirror in front of a conventional LDV optical system to scan the measurement volume perpendicular to the optical axis along an arc. Mean and RMS velocity profiles agreed well with pointwise measurements for low scan frequencies. The inertia of the oscillating mirror limited the scan frequency to about 15 Hz.

Owen (1984) developed a single velocity scanning LDV and made measurements in both water and air flows. A six-sided rotating polygon mirror was used and the scan rate was limited to 125 Hz due to restrictions on the data acquisition rates and the number of points required for one profile.

Improvements were suggested for a second phase of the work which will enable two-component real-time scans through high speed air flows. The disadvantage of a rotating mirror polygon is that the reflected beams are in unwanted directions 90% of the time.

Chehroudi and Simpson (1983) developed a single-component rapidly scanning LDV that scanned up to 150 Hz over 40 cm. The proper operation and usefulness of this design was demonstrated in a separated flow studied in a boundary layer wind tunnel. "Instantaneous" velocity profiles could not be obtained due to the data acquisition system used.

Antoine and Simpson (1986) extended the design above to a three-component system. A Ronchi ruling was used to produces fringe patterns in the horizontal plane to measure V. The fringe patterns produced by the Ronchi ruling were unsatisfactory.

Econonou extended the design of Chehroudi and Simpson (1983) to permit scans in the plane perpendicular to the mainstream flow velocity. This is a one component system and requires three scanners. For more information on this design see Econonou (1986).

1.3 Objective of this Work

The motivation for developing a rapidly scanning LDV is to obtain space-time data for and a better understanding of separated turbulent boundary

layers. The key to this understanding is in the instantaneous behavior of the large-scale structures which produce the large-scale diffusion of turbulence and momentum. A three component rapidly scanning LDV system would provide the necessary "instantaneous" velocity profile vital to understanding separating and separated turbulent boundary layers.

The behavior of these large-scale structures observed through the "instantaneous" velocity profiles would provide insight into a number of fundamental issues about separated turbulent flows. Among these issues are

1. the relationship between the large-scale structures and the on-set of instantaneous flow reversal.

2. the relationship between velocity and pressure fluctuations.

3. the relationship between large-scale structures and the lag and hysteresis of separated flows.

The almost instantaneous velocity profile provided by a three-component scanning LDV provides information to determine the inflows and outflows of turbulent kinetic energy and momentum and the many of the turbulent contributions to the pressure fluctuations. Such separated flow data cannot be obtained by hot-wire arrays because flow reversal or by image-processing of particle tracking photographs because of the three dimensional nature of such flows.

The objectives of the present work are as follows:

1. Develop a three-component rapidly scanning laser Doppler velocimeter (RSLDV) capable of scanning at least 40 cm or longer at high frequencies.

2. Develop a data acquisition system for the system above.

1.4 Outline of Thesis

Chapter 2 deals with the design of the RSLDV. The components of the transmitting optics are explained, as well as the problems with maintaining a coincident measuring volume over the scan length and techniques investigated to deal with this problem. The fringe patterns formed are also analyzed and discussed.

Chapter 3 describes the data acquisition and control hardware and logic.

Chapter 4 gives the conclusion of this work and makes recommendations for future work and improvements.

2.0 Description of RSLDV Optical Configuration

"Instantaneous" three-component velocity profiles are needed in order to gain a better understanding of separated turbulent flows. These velocity profiles would provide insight into the behavior of the large-scale structures which are responsible for the large-scale diffusion of turbulence energy and momentum.

Laser Doppler velocimetry should be used since it provides low uncertainty measurements and does not disturb the flow field. An LDV system to provide the necessary "instantaneous" velocity profiles should be capable of scanning a 40 cm height at rates of up to 300 scans/sec. The LDV system should provide concurrent measurements of all three velocity components using an on-axis beam arrangement, an on-axis system requires no modifications to the facilities at VPI&SU. The LDV system should also allow for variations in scan height, scan rate, location of the measurement volume, and the fringe spacing to be made easily.

The LDV system described below should fulfill these requirements.

2.1 General Description of Setup

As shown in Figure 1, the incoming beam from an Argon ion laser (λ = 514.5 nm) is directed by mirror (M1) to pass through a 20X laser beam expander (LBE). The expanded beam is then directed by mirror (M2) to pass through the focusing lens combination (L1 and L2). A dual water Bragg cell (BC) splits and frequency shifts the incoming beam. In the horizontal plane an unshifted and two shifted beams, a -30 MHz and a +30 MHz, are produced. A +15 MHz beam is produced for the vertical plane. Mirrors (M3 and M4) provide a longer path length before mirrors (M5a,b,c,d)to allow easy separation of the multiple beams. Mirrors (M5a,b,c,d and M6a,b,c,d) are used to steer the beams at the necessary angles onto the scanning mirror (SM) and also provide path length equalization between the four beams. The beams encounter additional optics after the scanning mirror (SM) necessary to produce the probe volume. Figure 2 shows the top and side view of the four beams intersecting to form the measurement volume. Figure 3 shows the on axis view of the four beams forming the measurement volume. These optics and the fringe patterns formed are described in the following sections.

Using the same optical setup, the laser can be used in a multi-mode operation to allow a two color (λ = 514.5 nm and 488 nm) LDV system with the addition of some color filters. Beam *A* would consist of both wavelengths, beams *B* and *D* of wavelength λ = 514.5 nm, and beam *C* of wavelength λ = 488 nm. The on axis view of the four beams forming the measurement volume for this

system is shown in Figure 4. The advantage of this arrangment is that there is more laser power in the measurement volume and only four fringe patterns are formed. With fewer fringe patterns the Doppler frequencies can vary more widely in frequency without overlapping.

2.1.1 Beam Expansion and Focusing Optics

The two lens combinations are used in order for the beams to cross at their waists, and to form an appropriate sized probe volume at the desired location in space.

The laser beam expander is positioned before the focusing lenses and is an Oriel laser beam expander modified to accept microscope objectives as the input lens, different microscope objectives can be used to achieve different beam expansion ratios. The beam expander allows adjustment of the spacing betweens its lenses, thus determining the size and divergence of the laser beam at the focusing optics. This determines the size of the probe volume, which influences fringe visibility and laser power density in the probe volume.

The focusing lenses determine the location of the beam waists and consist of positive achromatic lenses. The input beam size and divergence to this set of optics determines the size of the probe volume. The focal lengths and spacing between lenses are shown in Table 1.

The design of these two lens combinations depends upon several factors:

- The size of the probe volume necessary to maintain a coincident measuring volume (see 2.3 for more information).

- The minimum distance from the last lens set (L4) to the probe volume.

Since Guassian laser beams transform in a manner different form optical rays the normal thin lens equations (geometric optics) could not be used without large error (Yariv, 1985). Calculation of Guassian beam propagation through optical devices usually involves matrix transformations or 2-D Fourier transformations, which can be difficult to use. A more straight forward but less rigorous approach is given in Optics Guide 4 (1988).

In terms of input beam parameters:

$$\frac{1}{s+\frac{Z_R^2}{s-f}}+\frac{1}{s''}=\frac{1}{f} \qquad [2.1]$$

$$m=\frac{\omega''_0}{\omega_0}=\frac{1}{\sqrt{[1-\frac{s}{f}]^2+[\frac{Z_R}{f}]^2}} \qquad [2.2]$$

$$Z_R=\frac{\pi\omega_0^2}{\lambda} \qquad [2.3]$$

In terms of output beam parameters:

$$\frac{1}{s} + \frac{1}{s'' + \frac{Z''^2_R}{s'' - f}} = \frac{1}{f} \qquad [2.4]$$

where

s = object distance from lens

s'' = image distance from lens

f = focal length of lens

Z_R = Rayleigh range of input beam

Z''_R = Rayleigh range of output beam

m = magnification factor

ω_0 = input beam waist

ω''_0 = output beam waist

Lens combinations are handled by cascading the above equations; the image from the preceding lens is the object for the next lens in the optical system.

The design of the focusing lenses is considered first (see Figure 5). With the probe waist (ω''_{04}) and the location (d_{4p}) of the probe volume known and assuming reasonable values for f_3 and f_4 , the following equations result

$$s''_3 = \frac{f_3}{1 + \frac{\lambda f_3}{\pi \omega^2_{03}}} \qquad [2.5]$$

$$\omega''_{03} = \frac{\frac{\lambda f_3}{\pi \omega_{03}}}{\sqrt{1 + \frac{\lambda f_3}{\pi \omega_{03}^2}}} \qquad [2.6]$$

$$\frac{1}{d_{34} - s'' + \frac{Z_{R_4}^2}{d_{34} - s''_3 - f_4}} + \frac{1}{d_{4p}} = \frac{1}{f_4} \qquad [2.7]$$

$$m = \frac{\omega''_{04}}{\omega''_{03}} = \frac{1}{\sqrt{[1 - \frac{d_{34} - s''_3}{f_4}]^2 + [\frac{Z_{R_4}}{f_4}]^2}} \qquad [2.8]$$

Equations [2.7] and [2.8] are iteratively solved for the spacing between the two lenses (d_{34}) and the beam input waist (ω_{03}).

The beam expander optics is based on a reversed Keplerian telescope (see Figure 5). The equations for this lens system reduces to:

$$\frac{\omega_{01}}{\omega''_{02}} = \frac{f_1}{f_2}, \quad d_{12} = f_1 + f_2, \quad d_{23} = f_2 \qquad [2.9]$$

Since $\omega''_{02} = \omega_{03}$ and ω_{01} is the beam waist from the laser, selecting f_1 determines the value of f_2. The beam profile through the optical system shown in Figure 5 is for the $1/e^2$ beam intensity location, which is a hyperbolic function in the traverse direction (Yariv, 1985).

This optical configuration of expanding optics and focusing optics has advantages in the flexibility of adjusting the size and location of the probe volume independently.

2.1.2 Scanner

The G325DT scanner from General Scanning Inc. is a moving iron galvanometer with a position transducer designed specifically for closed-loop operation. This transducer operates by detection of capacitance variation between the rotating armature and a set of stationary electrodes. The controller includes a heater control regulating the temperature of the scanner. The mirror is a front surface mirror with DuAg coating, and is flat to one tenth of a wavelength over the useable aperture. The shaft wobble is typically below 5 arc-seconds and the signal response time is 10 ns.

2.1.3 Receiving Optics

The receiving optics consist of two cylindrical lenses (CL1,CL2), a long front surface mirror (M13), and the PMT, all assembled inside a black box having a side door for any adjustments (Figure 6). The first cylindrical lens (CL1) gathers light and enlarges the image of the measurement volume in the streamwise direction. The mirror deflects light onto the second cylindrical lens

(CL2) which constructs the image of the measurement volume on the PMT aperture for any positions of scan. Both lenses and mirror can be moved independently from each other in the vertical and horizontal direction. For more information on the design of the receiving optics see Antoine (1985).

2.2 *Horizontal Plane Optics*

To measure the velocity components in the horizontal plane (U and W), three beams are used. The optical configuration follows the same concept used in the designs of Chehroudi and Simpson (1983) and Antoine (1985). Beams *A* (unshifted), *B* (-30 MHz) and *D* (+30 MHz) form the probe volume to measure U and W velocity components (see Figures 1,2,3 and 4).

Beam *A* is reflected from the scanner to mirrors (M7,M8,M9a) to the probe volume. Mirrors (M7,M8) serve to equalize optical path length from the scanner to the probe volume. This assures coherence between the three beams and that the beams scan the same position. Beam *B* is reflected from the scanner to mirrors (M9b,M10,M11) and beam *D* to mirrors (M9d,M12,M13). The position and facing of mirrors (M10,M11,M12,M13) can be adjusted to allow changes in the horizontal fringe spacing and the position of the probe volume independently. Mirrors (M7,M8) are adjusted so that the path length from the scanner to the probe volume is equal for all three beams.

This optical arrangement allows changes in fringe spacing and the probe volume position to be independently made. Also, since each beam has its own set of optics, system alignment can be made individually for each beam uncoupled from the other beams. The path scanned by the three beams forming the horizontal plane probe volume is a vertical line.

2.3 *Vertical Plane Optics*

The vertical plane optics, necessary to measure the V component of velocity, proved to be the most difficult aspect in designing a three component rapidly scanning LDV system. There were two major problems that needed to be solved:

- The angle of intersection between the two beams forming the vertical plane probe volume should have a fringe spacing on the order of a few microns.

- The probe volume tends to scan an arc; coincidence of the horizontal and vertical probe volumes is difficult to achieve.

The length of the vertical plane probe volume (L_p) measured as the projection along the central beam (A) can be found as follows

$$L_p = \frac{\omega_{0p}}{\sin \phi} + \frac{\omega_{0p}}{\tan \phi} \qquad [2.10]$$

where

ϕ = angle of intersection between beams A and C

ω_{0p} = the beam waist at the measurement volume

Coincidence of the probe volumes is maintained when the path of the vertical plane probe volume is located within this area. Outlined below are several methods investigated to solve the coincidence problem.

2.3.1 Plane Mirror Pair

The simplest technique (and the basis for some of the other techniques) to form the vertical plane probe volume is to use two plane mirrors arranged as shown in Figure 7. Beam C (+15 MHz) is reflected from the scanner at an angle of θ_0 to beam A to mirror (M14), located at a distance of d_1 from the scanner and angle θ_1 to the horizontal plane. Mirror (M15), located at d_2 from the scanner and an angle of θ_2 to the horizontal plane, reflects beam C to intersect beam A to form the probe volume. Deriving ray equations for beams A and C

For beam A:

$$y = (x + x_0) \tan \theta \qquad [2.11]$$

For beam C:

$$\alpha = \theta_0 + \theta \qquad [2.12]$$

$$x_{M1} = d_1 \frac{\tan\theta_0 - \tan\theta_1}{\tan\alpha - \tan\theta_1} \qquad [2.13]$$

$$y_{M1} = x_{M1} \tan\alpha \qquad [2.14]$$

$$\beta = 2\theta_1 - \theta_0 - \theta \qquad [2.15]$$

$$\gamma = 2\theta_1 - \theta_0 \qquad [2.16]$$

$$x_{M2} = \frac{x_{M1}\tan\beta + d_1\tan\theta_0 - (d_1 - d_2)\tan\gamma - d_2\tan\theta_2 - y_{M1}}{\tan\beta - \tan\theta_2} \qquad [2.17]$$

$$y_{M2} = (x_{M2} - x_{M1})\tan\beta + y_{M1} \qquad [2.18]$$

$$\theta_r = -(2\theta_1 - 2\theta_2 - \theta_0 - \theta) \qquad [2.19]$$

$$y = (x - x_{M2})\tan\theta_r + y_{M2} \qquad [2.20]$$

Equation [2.11] gives the location of beam A at any scan angle θ , where x_0 is the difference between the path length of beam A from the scanner to the probe volume and the probe volume distance from the scanner. Equations [2.13,2.14] give the location of beam C on mirror (M14) and [2.17,2.18] on mirror (M15). The location of the beam intersection can be found by setting equation [2.11] and [2.20] equal to each other and solving for x.

$$x = \frac{y_{M2} - x_{M2} \tan \theta_r - x_0 \tan \theta}{\tan \theta - \tan \theta_r} \qquad [2.21]$$

Equations [2.21] and [2.11] give the x,y position of the vertical probe volume as the beams are scanned. From these two equations a solution for the five variables $(\theta_0, \theta_1, \theta_2, d_1, d_2)$ needs to be found that maximizes the vertical and horizontal probe volume coincidence. Since the horizontal probe volume scans a vertical line, a solution can be found by considering the minimization of the following integral

$$F = \int_0^{\theta_{max}} (x_p - x)^2 \, d\theta \qquad [2.22]$$

which can be viewed as the difference squared between the areas swept by the two probe volumes. An optimization algorithm, Sequential Linear Least Squares Programming (SLLSQP) (Kraft, *et al.* 1981), was used to find the minimum of equation [2.22]. No global minimum was found using this approach, even when θ_0 was held constant at a suitable value, due to the many peaks and valleys of many orders of magnitude across the domain space.

A brute force method was then used to find the minimum of eq. [2.22]; to reduce computer time and increase accuracy, the above equations were reformulated to reduce the number of free variables. To eliminate two of the variables, the beams were required to have an angle of intersection of ϕ and to cross at the required probe location x_p at a particular scan angle $\bar{\theta}$, in this case

$\frac{\theta_{max}}{2}$. This enables θ_2 and d_2 to be calculated in terms of the other variables as follows

$$\theta_2 = \frac{1}{2}(\phi - 2\theta_1 + \theta_0) \qquad [2.23]$$

$$d_2 = \frac{x_2 \tan\theta_2 - y_2 - x_1 \tan(2\theta_1 - \theta_0) + y_1}{\tan\theta_2 - \tan(2\theta_1 - \theta_0)} \qquad [2.24]$$

where

$$x_1 = d_1$$

$$y_1 = d_1 \tan\theta_0$$

$$x_2 = \frac{x_p \tan\theta_r(\bar{\theta}) - y_p - x_{M1}(\bar{\theta}) \tan\beta(\bar{\theta}) + y_{M1}(\bar{\theta})}{\tan\theta_r(\bar{\theta}) - \tan\beta(\bar{\theta})}$$

$$y_2 = (x_2 - x_p)\tan\theta_r(\bar{\theta}) + y_p$$

$$y_p = (x_p + x_0)\tan\bar{\theta}$$

The minimization algorithm increments d_1 across its domain while holding θ_1 and θ_0 constant; the computer program for this algorithm is in appendix A.1. The values of θ_2 and d_2 are calculated at each θ step via eqns. [2.23] and [2.24]. The value of F is calculated from eqns. [2.11 - 2.22]. The integral is approximated by using Simpson's rule. A minimum of F over the d_1 domain is obtained at each θ_1 step. The program can be run again with different θ_0 and ϕ values, some of the results are shown in Table 2.

The advantages of this optical arrangement are that it is simple and flexible: different probe volume locations and fringe spacing can be accommodated. The disadvantage is that coincidence is not maintained over a large scan length as can be seen from Figure 8.

2.3.2 Concave-Plane Mirror Pair

The path of the vertical probe volume formed by the two plane mirrors suggests that a concave mirror substituted for one of the plane mirrors would tend to converge the scan path closer to a vertical line. This optical arrangement can be seen in Figure 9. The development of the equations are similar to the above system

$$x_c = d_1 - R \sin \theta_1 \qquad [2.25]$$

$$y_c = d_1 \tan(\theta_0 + \theta_{max}) + R \cos \theta_1 \qquad [2.26]$$

$$x_{M1} = \frac{-b + \sqrt{b^2 - 4ac}}{2a} \qquad [2.27]$$

$$y_{M1} = x_{M1} \tan(\theta_0 + \theta) \qquad [2.28]$$

where

$$a = 1 + \tan^2(\theta_0 + \theta)$$

$$b = -2x_c - 2y_c \tan(\theta_0 + \theta)$$

$$c = x_c^2 + y_c^2 - R^2$$

$$\alpha = \theta_0 + \theta_{max} \qquad [2.29]$$

$$\delta = 2 \sin^{-1} \frac{\sqrt{(d_1 - x_{M1})^2 + (d_1 \tan \alpha - y_{M1})^2}}{2R} \qquad [2.30]$$

$$\beta = 2\theta_1 - \theta_0 - \theta_{\max} \qquad [2.31]$$

$$\gamma = 2(\theta_1 - \delta) - \theta_0 - \theta \qquad [2.32]$$

$$x_{M2} = \frac{(d_2 - d_1)\tan\beta + d_1 \tan\alpha - d_2 \tan\theta_2 + x_{M1}\tan\gamma - Y_{M1}}{\tan\gamma - \tan\theta_2} \qquad [2.33]$$

$$y_{M2} = (x_{M2} - x_{M1})\tan\gamma + y_{M1} \qquad [2.34]$$

$$\theta_r = -\left[2(\theta_1 - \delta) - 2\theta_2 - \theta_0 - \theta\right] \qquad [2.35]$$

The location of the center of the radius of curvature for the concave mirror is given by eqns. [2.25] and [2.26]. Beam C's location on the concave mirror is given by eqns. [2.27] and [2.28]. Equation [2.30] describes the relative change in angle with respect to θ_1 of the mirrors surface for the beam as it scans. The beam's position on the plane mirror is given by eqns [2.33] and [2.34].

Variables d_2 and θ_2 are again eliminated by using the method outlined in sec. 2.3.1. This results in the following

$$\theta_2 = -\frac{1}{2}(\phi - 2\theta_1 + \theta_0) \qquad [2.36]$$

$$d_2 = \frac{y_p - x_p \tan\theta_r(\theta_{\max}) - y_1 + x_1 \tan\gamma(\theta_{\max})}{\tan\gamma - \tan\theta_r(\theta_{\max})} \qquad [2.37]$$

where

$$x_1 = d_1$$

$$y_1 = d_1 \tan(\theta_0 + \theta_{max})$$

$$y_p = (x_p + x_0) \tan \theta_{max}$$

The beam intersection is found from eqn. [2.21] and the values above. The same type algorithm is employed to minimize F from eqn [2.22] except another loop is added to increment the radius of curvature for the concave mirror (see Appendix A.2). Some results are shown in Table 3 and Figure 10 shows the probe volume path for the minimum solution.

This technique results in better coincidence than that of the two plane mirrors, but changes in either the probe volume location or the fringe spacing may need a different concave mirror to obtain the best coincidence.

2.3.3 Prism

A prism, as shown in Figure 11, was another technique investigated to form the vertical plane probe volume. The following equations were derived considering the surface of the prism as a dielectric interface.

$$\alpha = \theta_0 + \theta \qquad [2.38]$$

$$\theta_1 = 90 - \theta_p + \frac{\varepsilon}{2} + \theta_0 + \theta \qquad [2.39]$$

$$\delta = \theta_1 + \sin^{-1}[\sqrt{(n^2 - \sin^2\theta_1)}\ \sin \varepsilon - \sin \theta_1 \cos \varepsilon] - \varepsilon \qquad [2.30]$$

$$\theta_2 = \sin^{-1}(\sin \frac{\theta_1}{n}) \qquad [2.41]$$

$$\beta = \theta_p - 90 - \frac{\varepsilon}{2} + \theta_2 \qquad [2.42]$$

$$\gamma = \theta_p - \frac{\varepsilon}{2} \qquad [2.43]$$

$$\psi = \theta_p + \frac{\varepsilon}{2} \qquad [2.44]$$

$$\theta_r = \theta + \theta_0 - \delta \qquad [2.45]$$

$$x_{s1} = \frac{D \tan(\theta_0 + \theta_{max}) - D \tan \gamma}{\tan \alpha - \tan \gamma} \qquad [2.46]$$

$$y_{s1} = x_{s1} \tan \alpha \qquad [2.47]$$

$$x_{s2} = \frac{D \tan(\theta_0 + \theta_{max}) - y_{s1} + x_{s1} \tan \beta - D \tan \psi}{\tan \beta - \tan \psi} \qquad [2.48]$$

$$y_{s2} = y_{s1} + (x_{s2} - x_{s1}) \tan \alpha \qquad [2.49]$$

$$x = \frac{y_{s2} - x_0 \tan \theta - x_{s2} \tan \theta_r}{\tan \theta - \tan \theta_r} \qquad [2.50]$$

The same type of algorithm is used to minimize F, see appendix A.3. Some results are shown in Table 4. This minimization technique did not work very well for this optical system, due to oversimplification in the optical system parameters.

2.3.4 Lens, Plane Mirror Pair

As shown in Figure 12, beam C passes through a plano-convex lens to the plane mirror system described in sec. 2.3.1. This method evolved from observation of the prism system above, a lens is used like a prism but provides a varying degree of deflection as the beam is scanned. The equations for this system are

$$x_L = \frac{d_L \tan(\theta_0 + \theta_{max}) - d_L \tan(90 + \theta_0 + \theta_{max})}{\tan(\theta_0 + \theta) - \tan(90 + \theta_0 + \theta_{max})} \qquad [2.51]$$

$$y_L = x_L \tan(\theta_0 + \theta) \qquad [2.52]$$

$$\varepsilon = \sin^{-1}\left[\frac{x_L - d_L}{R \sin(\theta_0 + \theta_{max})} \right] \qquad [2.53]$$

where

R = the radius of curvature of the lens $= f(n - 1)$

$$\delta = (\theta_{max} - \theta) + \sin^{-1}[\sqrt{n^2 - \sin^2(\theta_{max} - \theta)}\ \sin\varepsilon - \sin(\theta_{max} - \theta)\cos\varepsilon] - \varepsilon \qquad [2.54]$$

$$x_{M1} = \frac{x_L \tan(\theta_0 + \delta + \theta) - y_L + d_1(\tan\theta_0 - \tan\theta_1)}{\tan(\theta_0 + \delta + \theta) - \tan\theta_1} \qquad [2.55]$$

$$y_{M1} = x_{M1} \tan(\theta_0 + \delta + \theta) + y_L - x_L \tan(\theta_0 + \delta + \theta) \qquad [2.56]$$

$$\beta = 2\theta_1 - \theta_0 - \delta - \theta \qquad [2.57]$$

$$\gamma = 2\theta_1 - \theta_0$$

$$x_{M2} = \frac{(d_2 - d_1)\tan\gamma + x_{M1}\tan\beta + d_1\tan\theta_0 - d_2\tan\theta_2 - y_{M1}}{\tan\beta - \tan\theta_2} \qquad [2.58]$$

$$y_{M2} = (x_{M2} - x_{M1})\tan\beta + y_{M1} \qquad [2.59]$$

$$\theta_r = -(2\theta_1 - 2\theta_2 - \theta_0 - \delta - \theta) \qquad [2.60]$$

The variables d_2 and θ_2 are found from eqns [2.23] and [2.24], except they are evaluated at $\bar{\theta} = \theta_{max}$. The same algorithm is used to minimize F, eqn [2.22], with the focal length of the lens being changed for each run as necessary. Results are shown in Table 5 and Figure 13.

This technique maintains the best probe volume coincidence but requires more optical components, so set up is a little more complex. Changes in the probe volume location or fringe spacing can be made by changing the position and angles of the optics and may also require a different focal length lens for best results.

2.3.5 Dual Scanners

Another technique that can be used to maintain the coincidence of the probe volumes is to use two scanner. The second scanner would be located some

height, y_{s2}, above the primary scanner and would control the scan angle of beam C . The position output of the primary scanner would be used to drive the secondary scanner through a transfer function. The ideal transfer function is derived by determining the angle that beam C would have to be directed to intersect beam A at the probe volume, given by Eq. 2.11. This is developed as follows:

$$y = x \tan \theta_{s2} + y_{s2}$$

reqno [2.61] Setting Eq. 2.11 and 2.61 and solving for θ_{s2} gives:

$$\theta_{s2} = \tan^{-1}\left[\frac{(x + x_0) \tan \theta - y_{s2}}{x} \right] \qquad [2.62]$$

Figure 14 shows the relationship between the scan angles for the two scanners with the current setup. The position output from the scanners is a voltage linearly dependent on the scan angle. Also, the scan angle is linearly dependent on the input signal to the scanner control. Thus, the transfer function shown in Figure 14 applies to the position output signal and input signal for the two scanners.

This arrangement requires no addtional optics, besides the two scanners, and is easy to setup and align. Probe vloume coincidence can be maitained to a high degree, better than the above purely optical methods, by this method dependent on the accuracy that the transfer function could be implemented in an electronic circuit. However, scanner drift and non-linearities between scanner angle and postion output could be a problem.

2.4 *Doppler Frequencies for the System*

The interference phenomena between the four laser beams produces six moving fringe patterns for the single color system, as shown in Figure 3, and four moving fringe patterns for the two color system (see Figure 4), that permit the measurement of the U, V, and W components of velocity. These moving fringe patterns produce Doppler frequencies around 15 MHz, two 30 MHz, and 60 MHz; the single color system as additional Doppler frequencies around 15 MHz and 45 MHz. The Doppler frequencies can be determined by taking the dot product of unit vector of the moving fringe pattern with the velocity vector, this results in the following equations (see Figure 2)

$$\lambda_{BD}\,(f - 60\text{MHz}) = -\,U \qquad [2.61]$$

$$\lambda_{AB}\,(f - 30\text{MHz}) = -\,U\cos\frac{\alpha}{2} - (V - V_s)\sin\frac{\alpha}{2}\sin\theta + W\sin\frac{\alpha}{2}\cos\theta \qquad [2.62]$$

$$\lambda_{AD}\,(f - 30\text{MHz}) = -\,U\cos\frac{\alpha}{2} + (V - V_s)\sin\frac{\alpha}{2}\sin\theta - W\sin\frac{\alpha}{2}\cos\theta \qquad [2.63]$$

$$\lambda_{AC}\,(f - 15\text{MHz}) = (V - V_s)\cos(\frac{\phi}{2} - \theta) - W\sin(\frac{\phi}{2} - \theta) \qquad [2.64]$$

$$\lambda_{BC}(f-45\text{MHz}) = -U\frac{\sin\alpha}{2\sin\xi/2} + (V-V_s)\frac{\sin(\phi-\theta)+\cos\alpha\sin\theta}{2\sin\xi/2} + W\frac{\cos(\phi-\theta)-\cos\alpha\cos\theta}{2\sin\xi/2} \quad [2.65]$$

$$\lambda_{CD}(f-15\text{MHz}) = -U\frac{\sin\alpha}{2\sin\xi/2} - (V-V_s)\frac{\sin(\phi-\theta)+\cos\alpha\sin\theta}{2\sin\xi/2} - W\frac{\cos(\phi-\theta)-\cos\alpha\cos\theta}{2\sin\xi/2} \quad [2.66]$$

where

$$\xi = \cos^{-1}(\cos\alpha\cos\phi)$$

$$\lambda_{BD} = \frac{\lambda}{2\sin\alpha}$$

$$\lambda_{AB} = \lambda_{AD} = \frac{\lambda}{2\sin\alpha/2}$$

$$\lambda_{AC} = \frac{\lambda}{2\sin\phi/2}$$

$$\lambda_{BC} = \lambda_{CD} = \frac{\lambda}{2\sin\xi/2}$$

The above equations can be solved for velocity components U, V, and W in two ways. If the frequency difference between equations 2.62 and 2.63 can be obtained the following system of equations result

$$\begin{bmatrix} U \\ V-V_s \\ W \end{bmatrix} = \begin{bmatrix} -1 & 0 & 0 \\ 0 & \frac{\sin(\phi/2-\theta)}{2\sin\alpha/2\cos\phi/2} & \frac{\cos\theta}{\cos\phi/2} \\ 0 & \frac{\cos(\phi/2-\theta)}{2\sin\alpha/2\cos\phi/2} & \frac{\sin\theta}{\cos\phi/2} \end{bmatrix} \begin{bmatrix} \lambda_{BD}(f-60MHz) \\ \lambda_{AB}(f_{AB}-f_{AD}) \\ \lambda_{AC}(f-15MHz) \end{bmatrix} \quad [2.67]$$

The frequency difference can be obtained by bandpass filtering around 30 MHz, then squaring the resulting signal and low pass filtering, this can be performed analogically before sampling or digitally during processing. If the frequency difference between the two 30 MHz signals can not be obtained, then the following system of equations can be solved for the velocity components

$$\begin{bmatrix} U \\ V - V_s \\ W \end{bmatrix} = \begin{bmatrix} -1 & 0 & 0 \\ \cos\frac{\alpha}{2} & \frac{\mp \sin(\phi/2 - \theta)}{\sin \alpha/2 \cos \phi/2} & \frac{\cos \theta}{\cos \phi/2} \\ 0 & \frac{\mp \cos(\phi/2 - \theta)}{\sin \alpha/2 \cos \phi/2} & \frac{\sin \theta}{\cos \phi/2} \end{bmatrix} \begin{bmatrix} \lambda_{BD}(f - 60MHz) \\ \lambda_{AB}(f - 30MHz) \\ \lambda_{AC}(f - 15MHz) \end{bmatrix} \quad [2.68]$$

In the equation above the minus sign (-) refers to the Doppler frequency from eqn [2.62] and the plus sign (+) to eqn [2.63]. For the single color system additional signals around 15 MHz and 45 MHz (eqns. 2.65,2.66) are present. With these two equations and the U velocity component calculated from one of the system of equations above, a second set of estimates for the V and W velocity components can be obtained. The two sets of estimates can then be averaged.

2.4.1 Uncertainty Analysis

An uncertainty analysis can be performed on the velocity estimates calculated from the equations above using a method given in Holman (1984).

We wish to estimate the uncertainty in the result R on the basis of the uncertainties in the primary measurements. The result R is a giver function of independent variables $x_1, x_2, ..., x_n$. Thus,

$$R = R(x_1, x_2, ..., x_n) \qquad [2.69]$$

The uncertainty in R, w_R, given the uncertainty in the independent variables, $w_1, w_2, ..., w_n$, is given by

$$w_R = \left[\left(\frac{\partial R}{\partial x_1} w_1 \right)^2 + \left(\frac{\partial R}{\partial x_2} w_2 \right)^2 + ... + \left(\frac{\partial R}{\partial x_n} w_n \right)^2 \right]^{1/2} \qquad [2.70]$$

It should be noted that the uncertainty in the independent variables for this uncertainty analysis method are at the same given odds and that the variables are assumed to be normally distributed. The partial derivatives in the equation [2.70] above can be approximated by

$$\frac{\partial R}{\partial x_i} \simeq \frac{R(x_1, x_2, ..., x_i + \Delta x_i, ...x_n) - R(x_1, x_2, ..., x_i, ...x_n)}{\Delta x_i} \qquad [2.71]$$

This is useful when the data reduction is rather complicated and the analytical derivatives are difficult to derive.

The uncertainty analysis described above will be applied to the two color RSLDV setup with velocity estimates calculated from equation [2.67]. For illustrative purposes the following setup parameters will be used.

Beam intersection angles:

$$\alpha = 6^\circ \pm 0.5\ \%$$

$$\phi = 10^\circ \pm 0.5\ \%$$

Fringe spacings:

$$\lambda_{BD} = 2.46\ \mu\text{m} \pm 0.1\ \%$$

$$\lambda_{AB} = \lambda_{AD} = 4.92\ \mu\text{m} \pm 0.1\ \%$$

$$\lambda_{AC} = 2.8\ \mu\text{m} \pm 0.1\ \%$$

Scan velocity

$$V_s = 60 \pm 0.05\ \text{m/s}$$

and the scan angle will be taken as:

$$\theta = 0^\circ \pm 0.01^\circ$$

We will consider a case where the signal-to-noise ratio (SNR) of the PMT signal is 20 dB and signal processing is performed via the fast Fourier trasnform (FFT) with zero-padding and log-parabolic interpolation algorithm (Shinpaugh, 1989) with 1024 points in the data set. The uncertainty in the frequency estimates based on this algorithm and SNR is $\pm$10 KHz. The laser wavelengths and the Bragg cell frequencies are known with enough accuracy that they make negligible contribution to the overall velocity uncertainties.

For this analysis we consider the flowfield around a wing-body junction flow, from which we can determine a worst case and best case senario. The worst case will occur for the following velocity componets:

U = $\pm$30 m/s, V = -2 m/s, and W = 16 m/s

and the best case will be for:

U = 0 m/s, V = 2 m/s, and W = 0 m/s

The partial derivatives of the velocity estimates from eqn. [2.67] were calculated analytically with respect to the variables α, ϕ, θ, λ_{BD}, λ_{AB}, λ_{AC}, f, and V_s . Using the values given above for independent variables and their uncertainties in eqn. [2.70] we can calculate the worst and best case uncertainties in the velocity component estimates. For the worst case we obtain the following results:

U = 30 $\pm$0.04 m/s

V = -2 $\pm$0.1 m/s

W = 16 $\pm$0.47 m/s

and at best the uncertainties will be

U = 0 $\pm$0.02

V = 2 $\pm$0.1 m/s

W = 0 $\pm$0.47 m/s

However, through careful calibration it may be possible to reduce these uncertainties in the velocity estimates to some degree.

3.0 Data Acquisition and Control System

Ideally, in a scanning LDV system one needs to know the exact position of the measurement volume at the time when a "validated" velocity measurement is detected. Since the PMT signal contains six Doppler frequencies in high noise, this precludes the use of an online signal processing system. Therefore, the PMT signal needs to be digitized and stored, along with the position of the measurement volume, for later processing. Figure 15 shows the general layout for such a data acquisition and control system, each of the elements are described below.

3.1 IBM PC-RT Computer

The computer features a 32 bit RISC (Reduced Instruction Set Computer) technology CPU, 16 Megabytes of fast memory and AT compatible data bus and

card slots. The machine runs under AIX 2.2.1 which is a UNIX based operating system. Two 400 MB DASD (Direct Access Storage Device) drives and a 940 megabyte optical disk drive are connected to the RT via a SCSI (Small Computer Systems Interface) adapter. The two DASD drives provide online storage of LDV data during data acquisition and the optical disk drive provides permanent storage of the LDV data. Sustained data write rates of up to 410 KB/sec are possible using the DASD drives and the SCSI interface.

A Jorway corp. SCSI CAMAC controller interfaces the RT and the two transient recorders. Data transfer rates of up to 1.5 MB/sec are possible over this interface.

3.2 Transient Recorders

Both transient recorders, from the LeCroy corporation, have the TR8828c digitizer. This digitizer samples at 200 mega-samples/sec with 8 bit resolution and 100 MHz bandwidth. The transient recorder used to record the PMT signal has 16 MB of memory, the other transient recorder has 32 KB of memory and is used to record the position output from the scanner control.

3.3 *Array Processor*

The array processor is a ZIP 3232-20 from Mercury Computer Systems. This system features 20 MFLOP performance, 2 MB of fast memory and a 40 MB/sec data way. Built in software routines are callable from fortran and new algorithms can be programmed via a software interface. A 1024 point real (non-complex data) FFT (fast Fourier transform) can be computed on this system in 1.3 msecs.

3.4 *Data Acquisition Procedure*

The whole data acquisition procedure is designed to minimize the amount of time required to gather a statistically significant record length, about 5 seconds or more of data. This is done so that variations in the tunnel properties can be minimized during the data acquisition procedure. A total of 80 transient recorder records are taken, this is about 1.25 gigabytes of data.

The RT computer controls the entire data acquisition and transfer process. Both transient recorders are triggered at the same time when the measurement volume is beginning a scan. Data is taken continuously until the transient recorder sampling the PMT signal has filled the 16 MB of memory, which sends a memory full signal to the RT over the GPIB interface. The RT then reads the

memory from the transient recorder and writes this data to a file on the DASD disks; this operation takes approximately one minute to complete. Once the entire 16 MB of memory has been transferred, the RT reads the memory of the other transient recorder containing the scan position and writes this data to a file. The whole process is repeated until the desired number of records has been obtained.

The files are stored with a sequential type file name, so the order of the files can be maintained. Also stored at the beginning of each file is the system time so that the exact time of each velocity realization can be easily determined. The data can be stored permanently to the optical disk once all the data has been collected; more data can be taken at another scan location or the data can be processed.

Using one of the signal processing algorithms given by Shinpaugh (1989), the data is read from disk and transferred to the array processor to determine the velocity of any Doppler bursts in the record. During processing, the computer keeps track of the time and location of each velocity measurement.

3.5 Seeding

In order to improve the signal-to-noise ratio of the received Doppler signals mono-dispersed polylatex spheres will be used for seeding. By using mono-dispersed particles the seeding level can be adjusted so that there is on

average only one particle in the measurement volume at one time, thus avoiding the noise generated by having multiple submicron particles in the measurement volume typically with other seeding techniques. Also with monodispersed particles it is possible to determine the path through the measurement volume by the relative intensity of the signal.

The polylatex spheres are mixed with either alcohol or water to get a mixture that is approximately 0.25% by weight. An aerosol is generated from this mixture by a seeder similar to the design of Echols and Young (????). The aerosol is introduced into the boundary layer near the begining of the tunnel; this allows time for the particles to dry before reaching the measurement volume. To reduce particle clumping the percent solids of the solution can be adjusted.

4.0 Conclusions and Recommendations for Future Work

4.1 Conclusions

A rapidly scanning three-velocity-component laser Doppler velocimeter has been designed, to obtain near instantaneous velocity profiles in complicated three dimensional flows.

The optical configuration allows the size and location of the measurement volume, as well as all the fringe spacings to be varied freely. The four beams have independent lens and mirror sets to avoid coupling, making system alignment easier, changes made for one beam do not affect another. Path equalization is maintained. Techniques to maintain coincidence between the vertical and horizontal probe volumes were investigated. The lens, plane-mirror pair maintained the highest level of coincidence between the two probe volumes, and

an appropriate lens has been manufactured by a local optician for use with the RSLDV.

Six moving fringe patterns at (2x) 15, (2x) 30, 45, and 60 MHz are produced by two Bragg cells for the single color system. For the two color system, moving fringe patterns at 15, (2x) 30, and 60 MHz are produced by the two Bragg cells. The signal around 60 MHz is a direct measurement of the U velocity, and the signal around 15 MHz and the frequency difference between the two 30 MHz signals are used to calculate the V and W velocity components. An uncertainty analysis applied to the system of equations used to calculate the velocity components with a worst case senario, the uncertainties in U, V, and W velocity estimates are ± 0.04 m/s, $\pm$ 0.1 m/s, and ± 0.47 m/s respectively.

A data acquisition, control and processing system has also been designed for use with the RSLDV. The PMT signal is sampled at 200 MB/sec by a transient recorder and the position of the scanner is also recorded by a transient recorder. The data from the transient recorders is transferred over a GPIB interface to a mini-computer for storage, the data transfer rate is at 300 KB/sec. Online storage is provided for up to 1.25 gigabytes of data, this translates into 6 seconds worth of LDV data. Permanent storage is provided by an optical disk drive.

4.2 *Recommendations for Future Work*

Now that an appropriate design has been made for a rapidly scanning three-velocity-component laser Doppler velocimeter, additional optics can be acquired and the system setup. The final setup may require some changes in a few of the configuration parameters, but these adjustments should be minor. The quality of the fringe patterns can then be observed and the system can be calibrated by using a rotating disk. The RSLDV will then be used to investigate some well documented turbulent flows in the Virginia Tech Boundary Layer Wind Tunnel, including some steady and unsteady separated flows and a wing-body junction flow.

Improvements to the optical system should be made on increasing the coincidence between the horizontal and vertical probe volumes. This could be accomplished by using a glass wedge of the proper shape, instead of the current lens, an elliptical or parabolic mirror or by using another scanner to scan the upper beam with a feedback control from the original scanner. By improving the coincidence between the two probe volumes, the size of the measurement volume can be decreased, leading to improved resolution and higher SNR for the signal from the PMT.

In an extension to the current design of the RSLDV, a pockel cell can be placed just after the Bragg cells. This permits two parallel scan lines that are separated by a small distance, ΔY (about 6 mm), in the freestream direction. The pockel cell is switched on and off, synchronized with the up-and-down scanning

of the measurement volume. The measurement volume is scanned up at one x_1 location while scanning down at an other x_2 location. This permits information on the streamwise changes in the flow to be obtained. Two separate PMTs would be needed in this arrangement.

References

Antoine, M., "A Rapidly Scanning Three-Velocity-Component Laser Doppler Anemometer", *MS Thesis, Dept. of Aerospace and Ocean Eng., VPI & SU*, Blacksburg, VA, 1985.

Antoine, M. and Simpson, R.L. , "A Rapidly Scanning Three-Velocity-Component Laser Doppler Anemometer", *J. Physics E: Sci. Inst., 19*, pp. 853-858, 1986.

Bendat, J.S., and Piersol, A.G., *Random Data Analysis and Measurement Procedures, 2nd ed.*, John Wiley and Sons, New York, 1986.

Bendick, P.J., "A Laser Doppler Velocimeter to Measure Instantaneous Velocity Profiles", *Proc. Flow Symposium*, Pittsburgh, PA, 1971.

Chehroudi, B. and Simpson, R.L., "A Rapidly Scanning Laser Doppler Anemometer", *Report WT-7, Dept. Civil/Mechanical Engr.*, Southern Methodist Univ., Dallas, Tx 75275: DTIS Report, 1983.

Durst, F., Lehmann, B., and Tropea, C., "Laser Doppler Systems for Rapid Scanning of Flow Fields", *Rev. Sci Instr., vol 52*, pp 1076-1681, 1981.

Durst, F., Melling, A., and Whitelaw, J.H., *Principles and Practices of Laser Doppler Anemometry*, 2nd ed., Academic Press, New york, 1981.

Econonou, M., "Design and Performance of a Scanning Laser Doppler Velocimeter", *MS Thesis, Mech. Eng., Ill. Inst Tech.*, Chicago, 1986.

Gartell, L.R., and Jordan, F.J., "Demonstration of a Rapid-Scan Two-Dimensional Laser Velocimetry in the Langley Vortex Research Facility for Research in Aerial Applications", *NASA TM-74081*, 1977.

Grant, G.R., and Orloff, K.L., "Two-Color Dual-Beam Backscatter Laser Doppler Velocimeter", *J. of Applied Optics, vol 12*, pp. 2913-2916, 1973.

Holman, J.P., *Experimnetal Methods for Engineers*, McGraw-Hill, New York, 1984.

Kraft, D., Oberpfaffenhofen, D., Schittkowski, K., "Sequentail Linear Least Squares Programming", Univ. Wuerzburg, 1981.

Optics Guide 4, Melles Griot, 1988.

Meyers, J.F., "Application of Laser Velovimetry to Large Scale and Specialized Aerodynamic Tests", *TST Quart., vol 5, iss 4*, pp 5-12, 1979.

Nakatani, N., Yorisue, R., and Yamada, T., "Simultaneous Measurements of Flow Velocities in Multipoint by the Laser Doppler Velocimeter", *Proc. Dynamic Flow Conf.*, pp 583-590, Marseille-Baltimore, 1978.

Nichols, C.E., Jr., "Preparation of Polystyrene Microspheres for Laser Velocimetry in Wind Tunnels", , *NASA TM 89163*, 1987.

Orloff, K.L., and Biggers, J.C., "Laser Velocimeter Measurements of Developing and Periodic Flows", *Proc. 2nd Int. Workshop on LDV, 2*, pp 143-168, Purdue University, 1974.

Orloff, K.L., Corsiglia, V.R., Biggers, J.C., and Ekstedt, T.W., "The Accuracy of Flow Measurements by Laser Doppler Methods", *Proc. LDA Symp.*, pp 624-643, Copenhagen, 1975.

Owen, F.K., "A Scanning Laser Velocimeter for Turbulence Research", *NASA Contractor Report 172493*, 1984.

Rhodes, D.B., "Optical Scanning Systems for Laser Velocimeter", *SPIE, vol 84*, pp 78-84, 1976.

Simpson, R.L., "Scanning Laser Anemometry and Other Measurement Techniques for Separated Flows", *Advances in Fluid Mechanics Measurements Lecture Notes in Engineering*, Vol. 45, pp. 357-400, ed. M. Gad-el-Hak, Springer-Verlag, New York, 1989.

Shinpaugh, K.A., "Design of a 3-D Rapidly Scanning Laser Doppler Velocimeter with Low SNR Signal Processing", *MS Thesis, Department of Aerospace and Ocean Engr., VPI&SU*, Blacksburg, VA, 1989.

Yariv, A., *Optical Electronics*, Holt, Rinehart and Winston, Inc., New York, 1985.

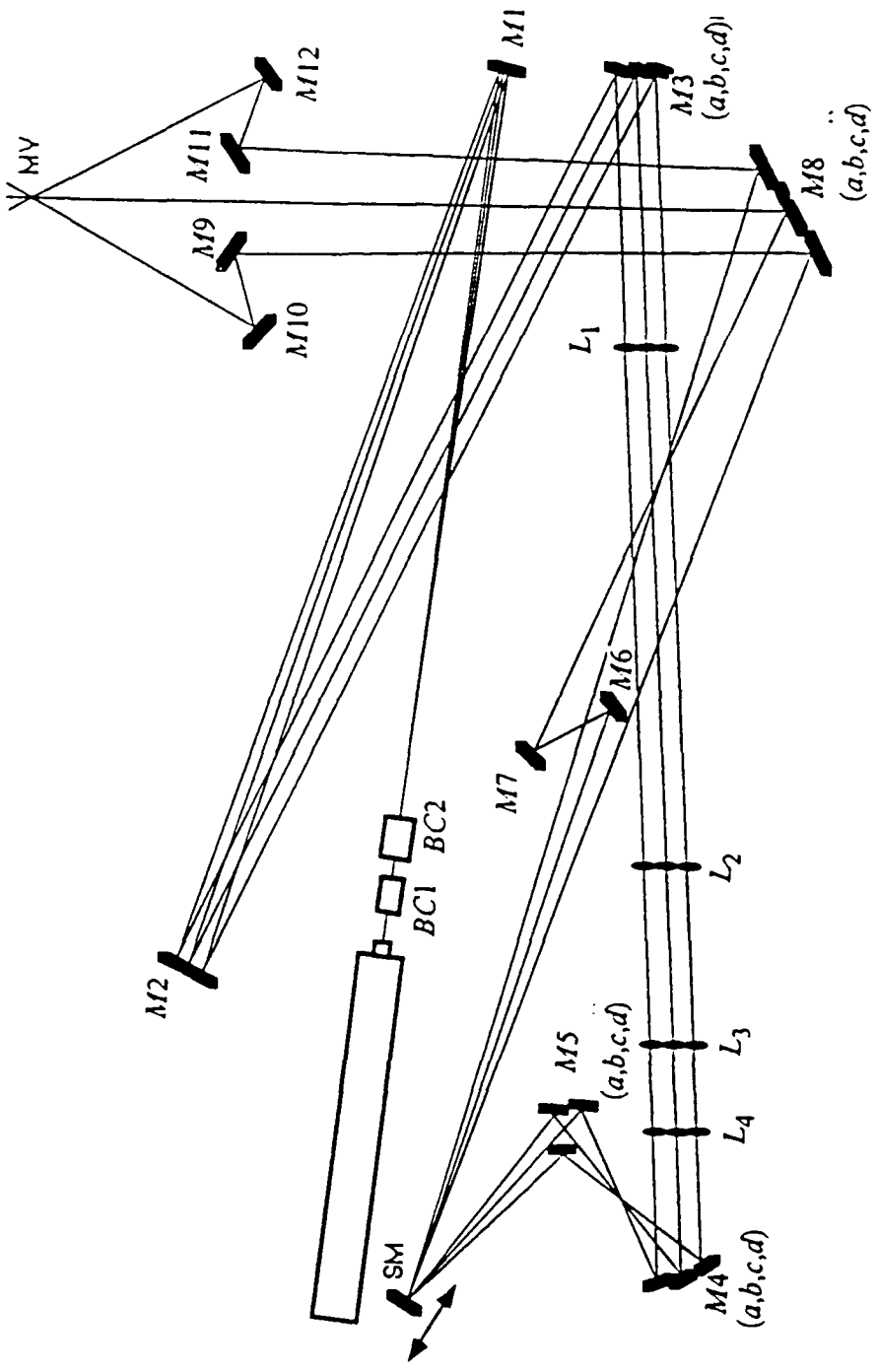

Figure 1. Top View of Optical Configuration of the RSLDV System.

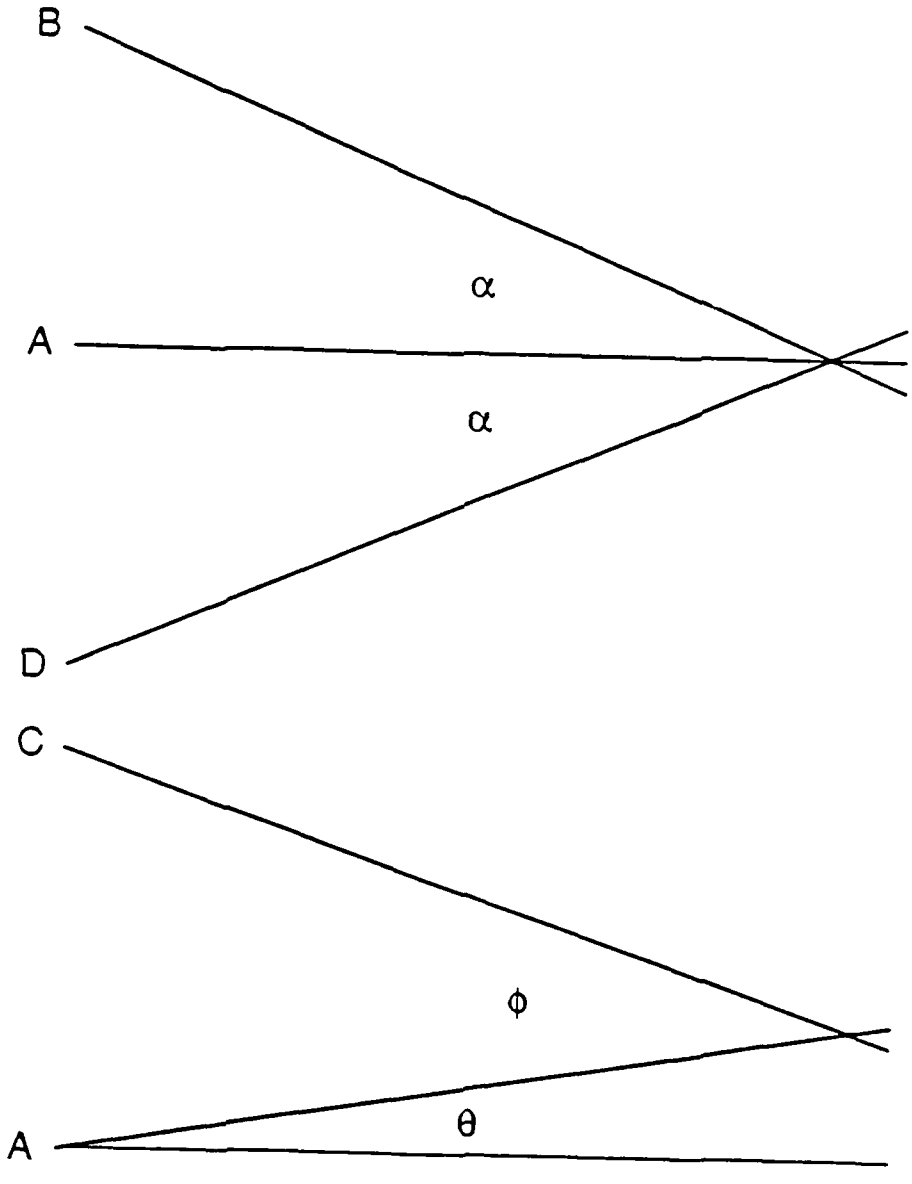

Figure 2. Top and Side View of the Four Beams Intersecting to form the Measurement Volume.

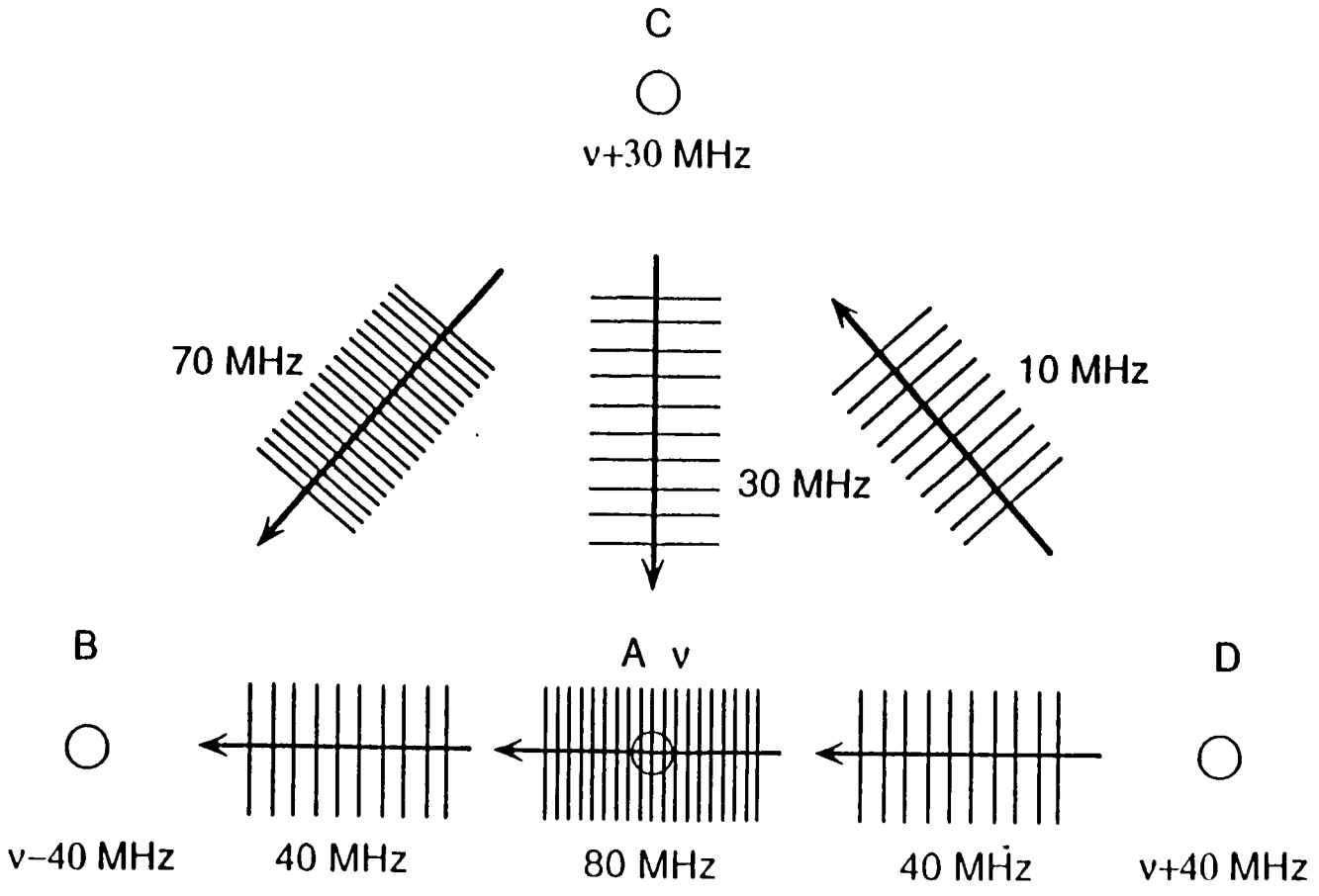

Figure 3. On-axis View of the Four Beams forming the Measurement Volume for the Single Color System.

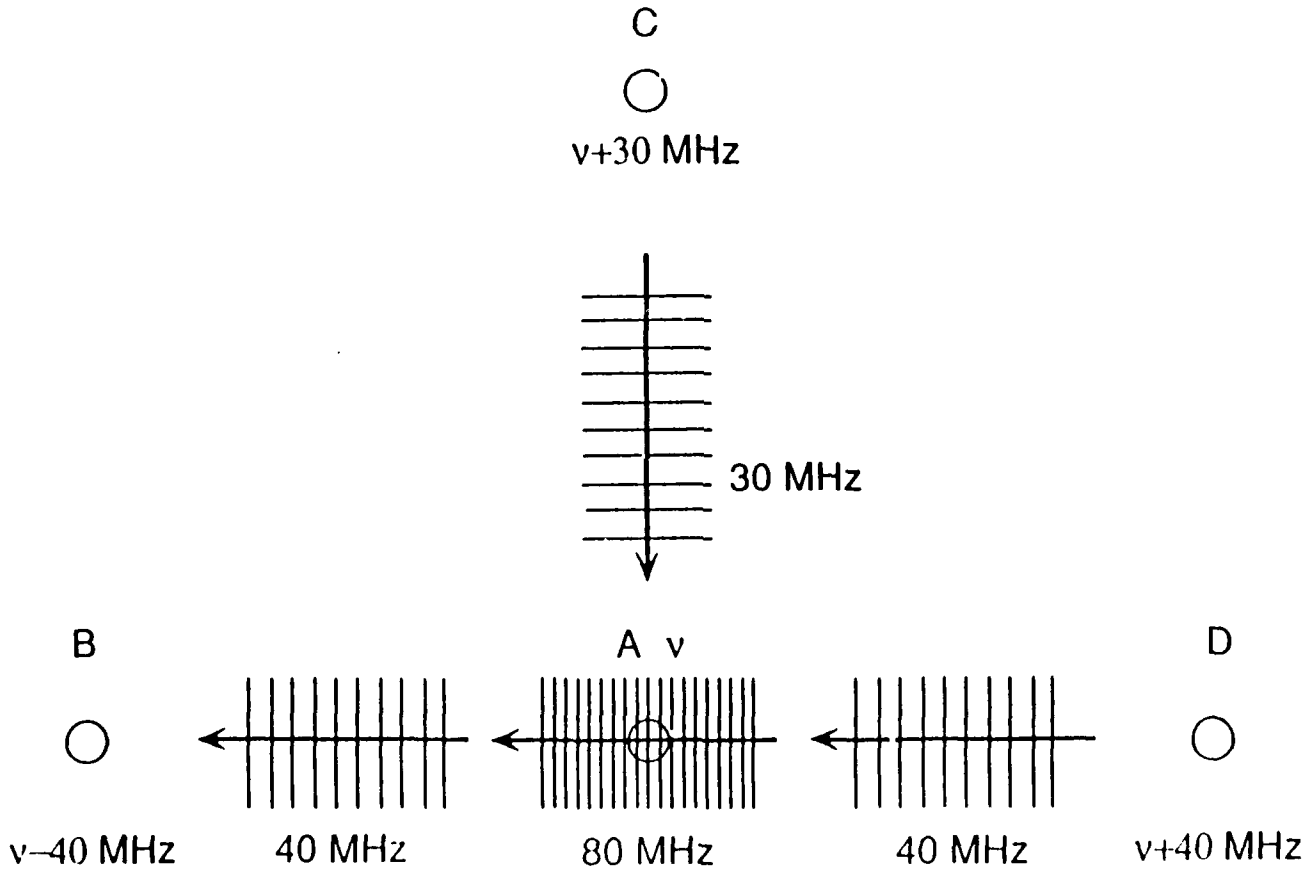

Figure 4. On-axis View of the Four Beams forming the Measurement Volume for the Two Color System.

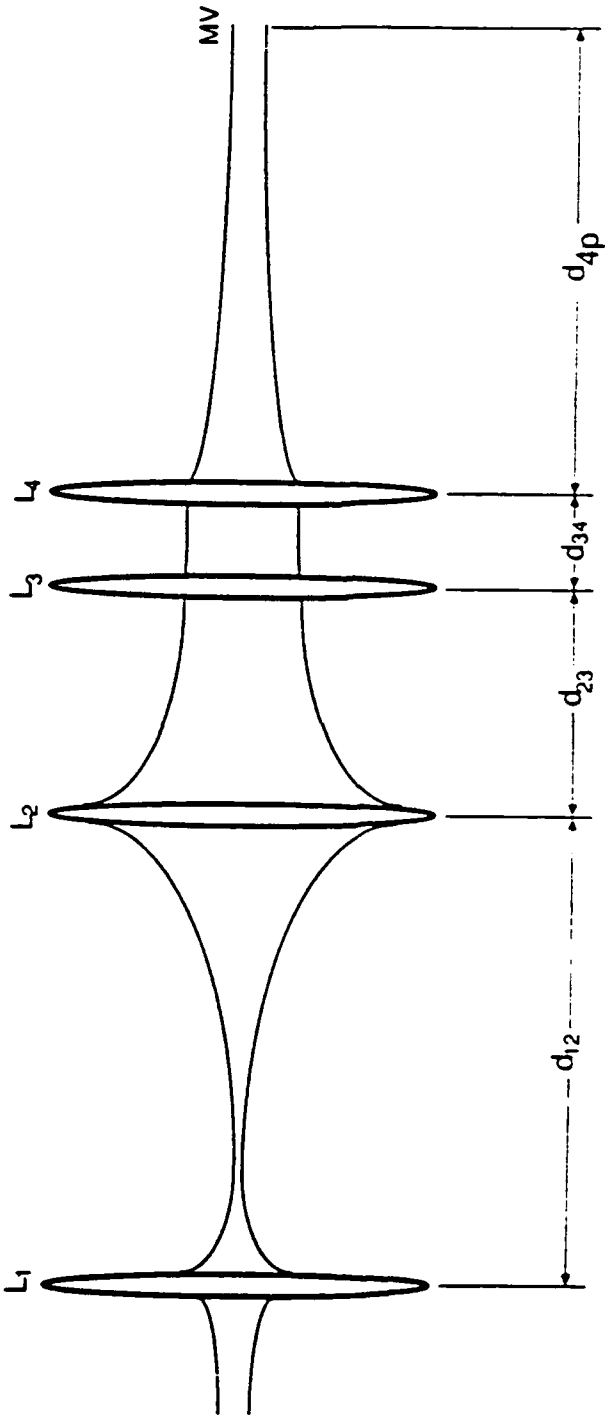

Figure 5. Side View of Transmitting Lens Configuration.

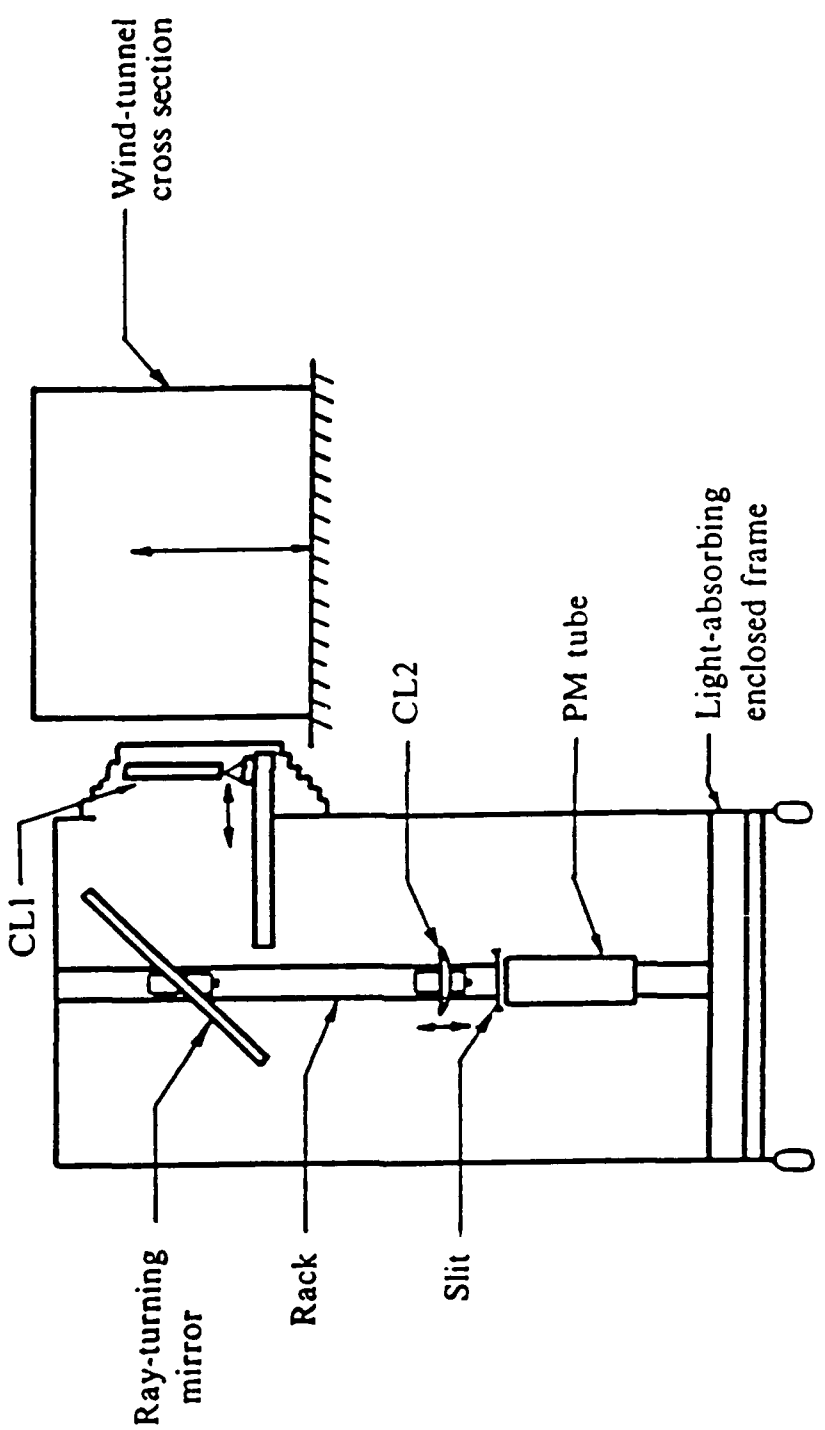

Figure 6. Receiving Optics Schematic Diagram.

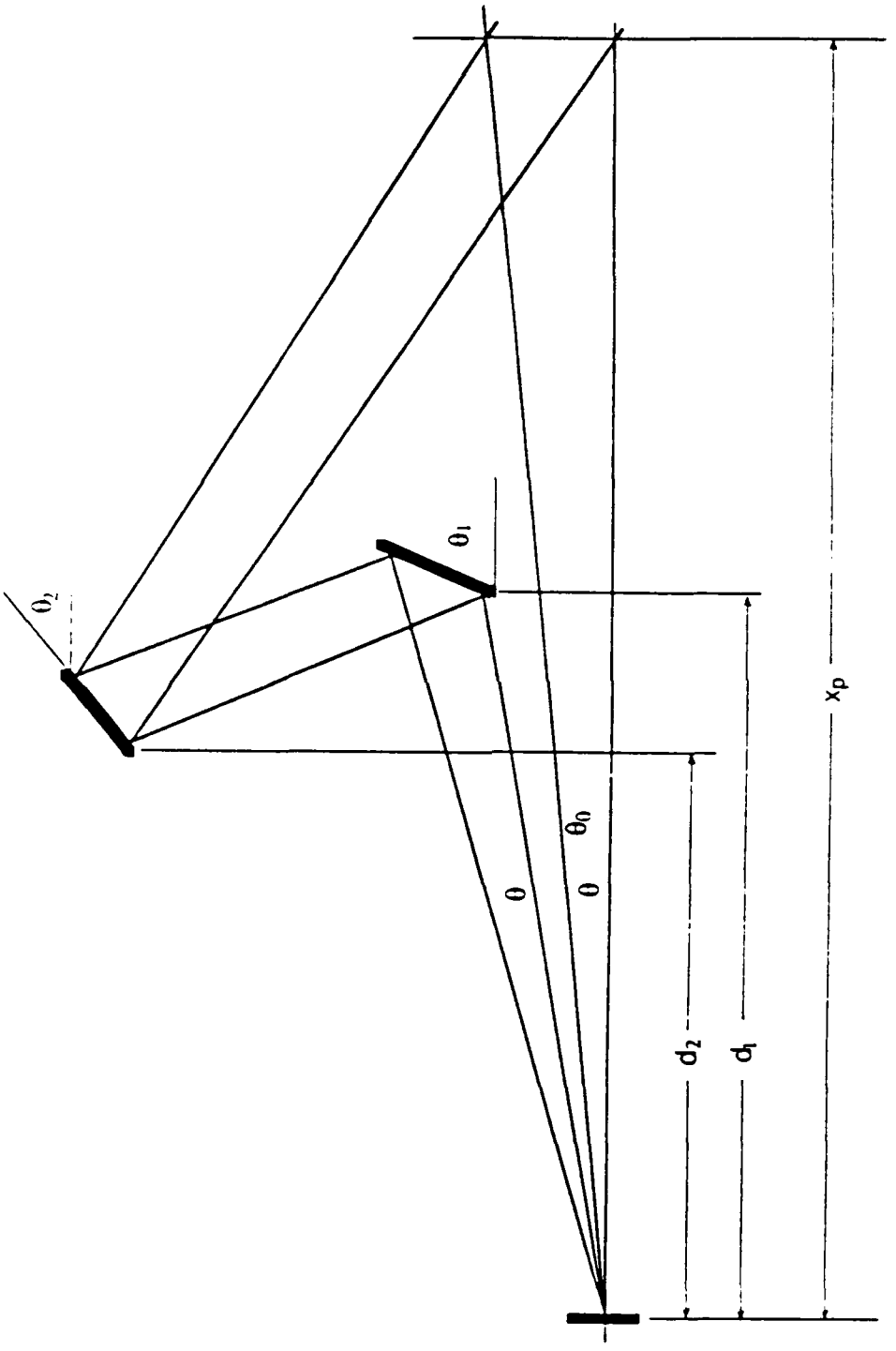

Figure 7. Side View of Vertical Plane Optics: Plane Mirror Pair.

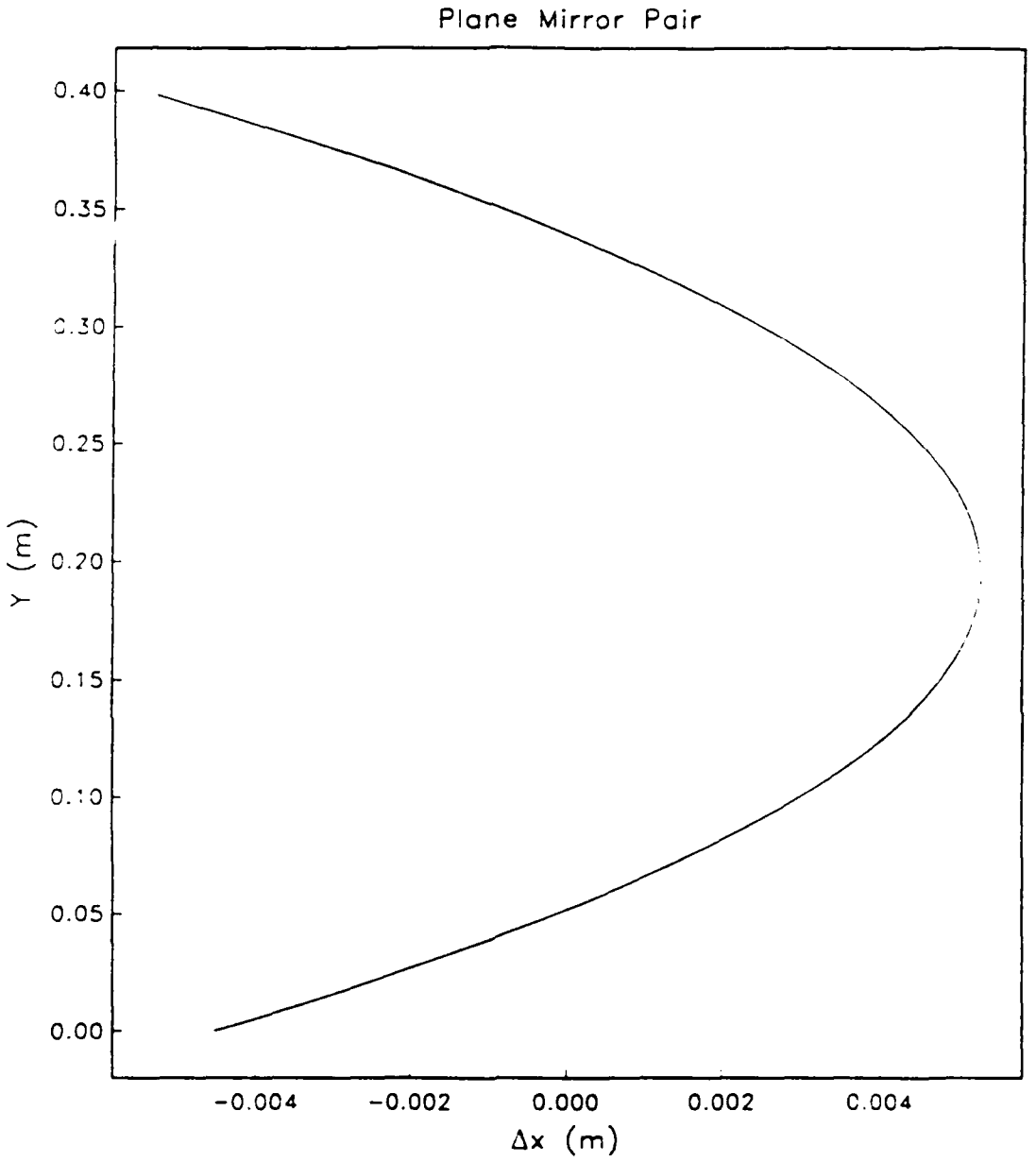

Figure 8. Scan Path of Probe Volumes: Plane Mirror Pair.

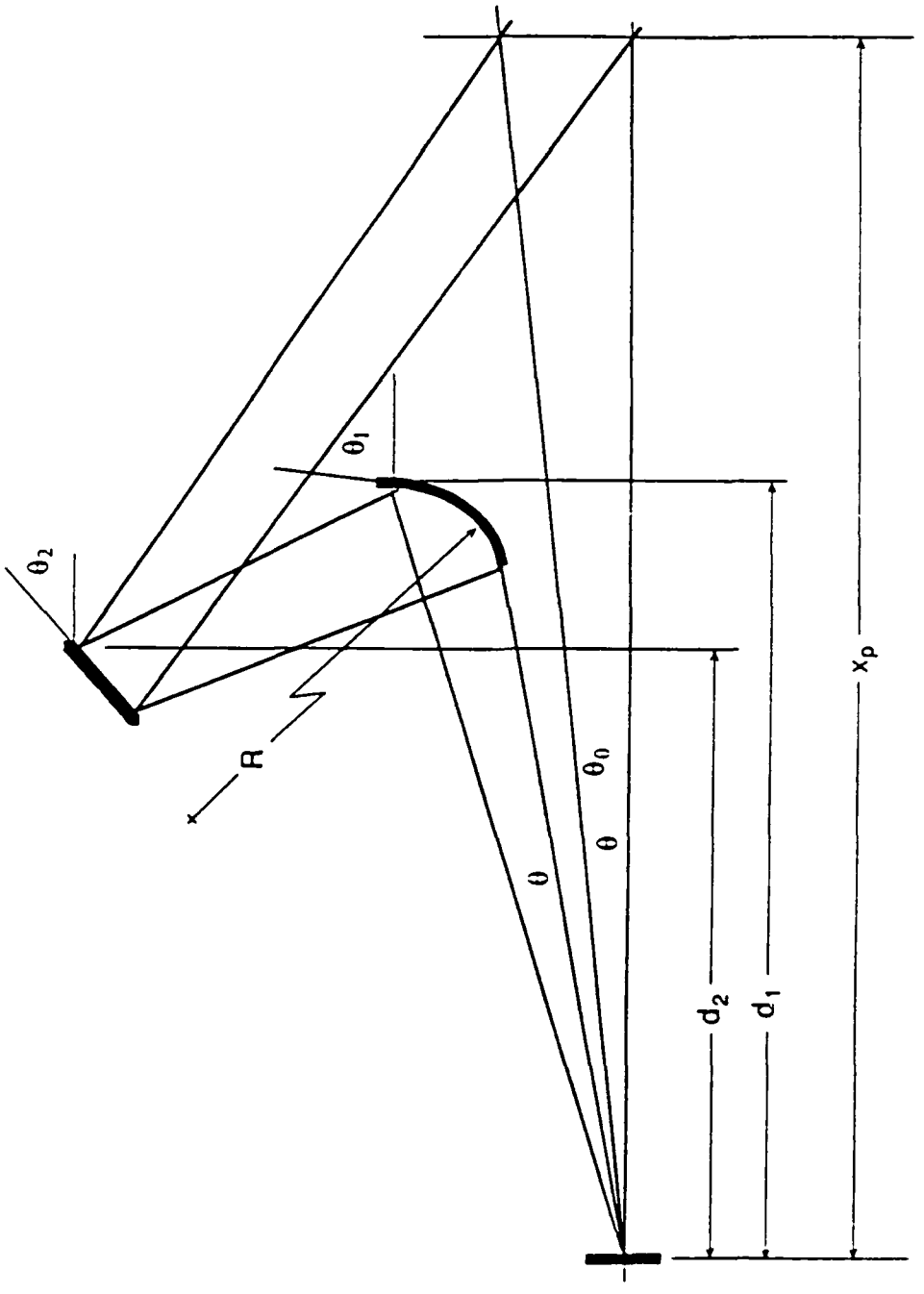

Figure 9. Side View of Vertical Plane Optics: Concave-Plane Mirror Pair.

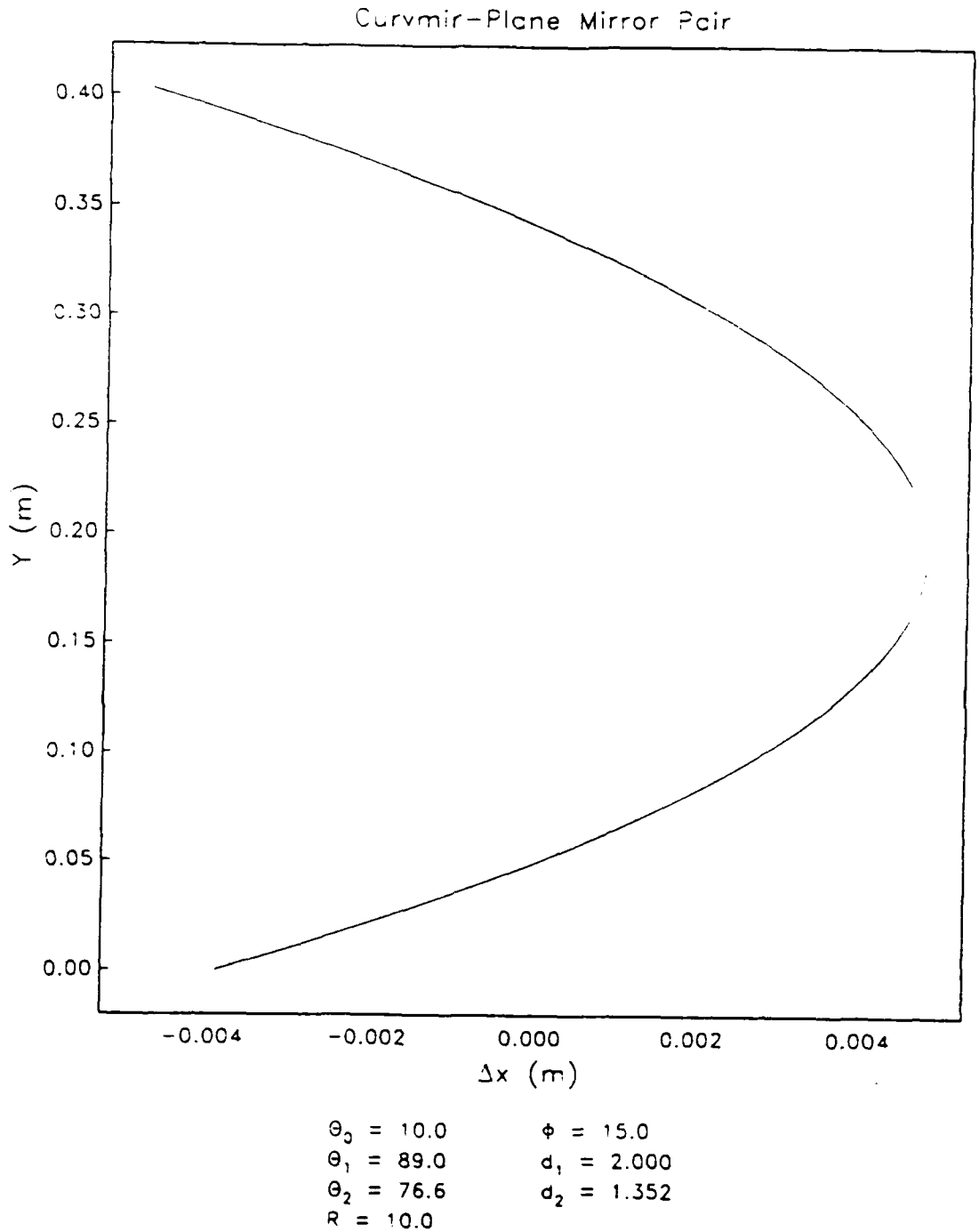

Figure 10. Scan Path of Probe Volumes: Concave-Plane Mirror Pair.

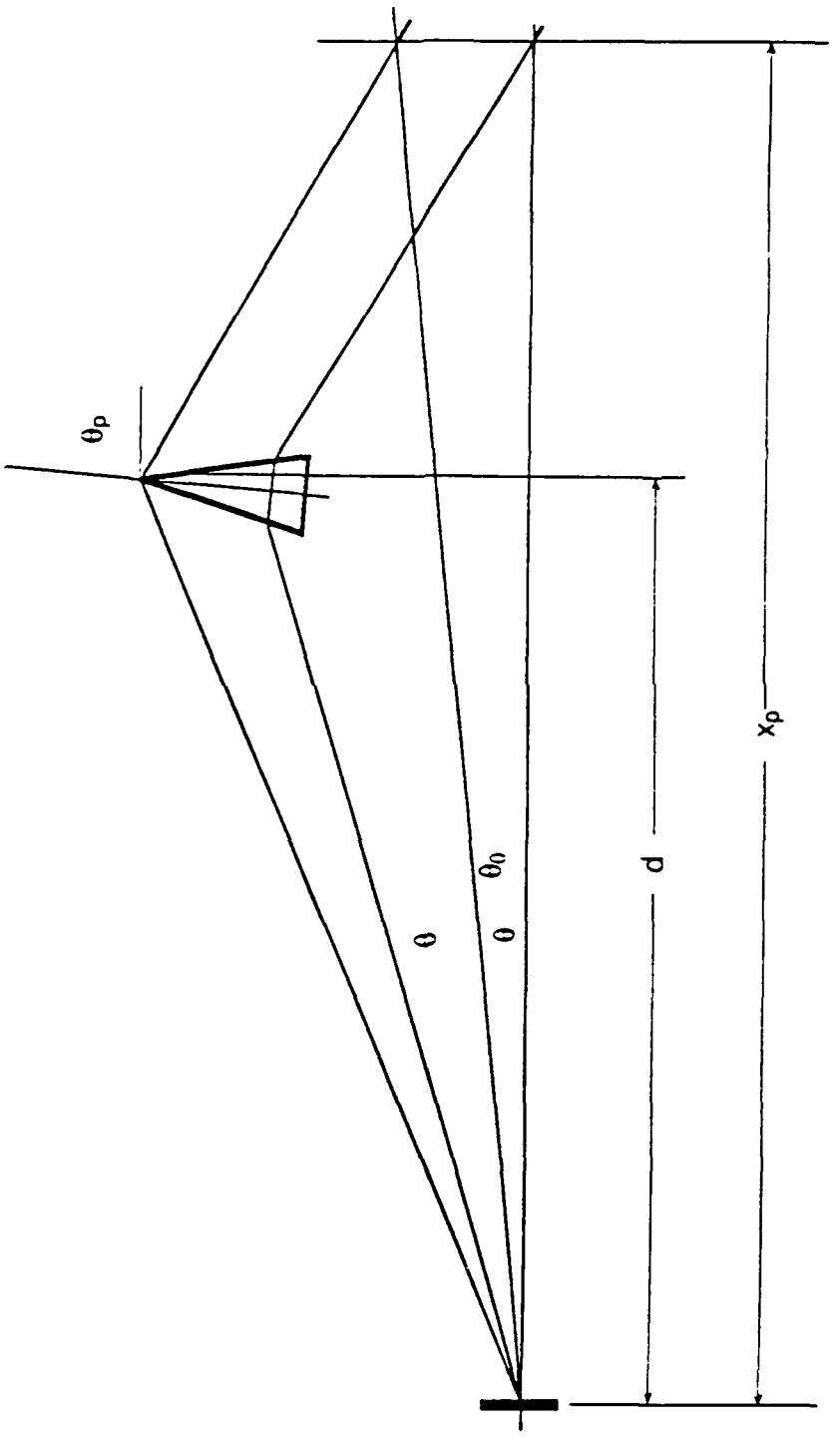

Figure 11. Side View of Vertical Plane Optics: Prism.

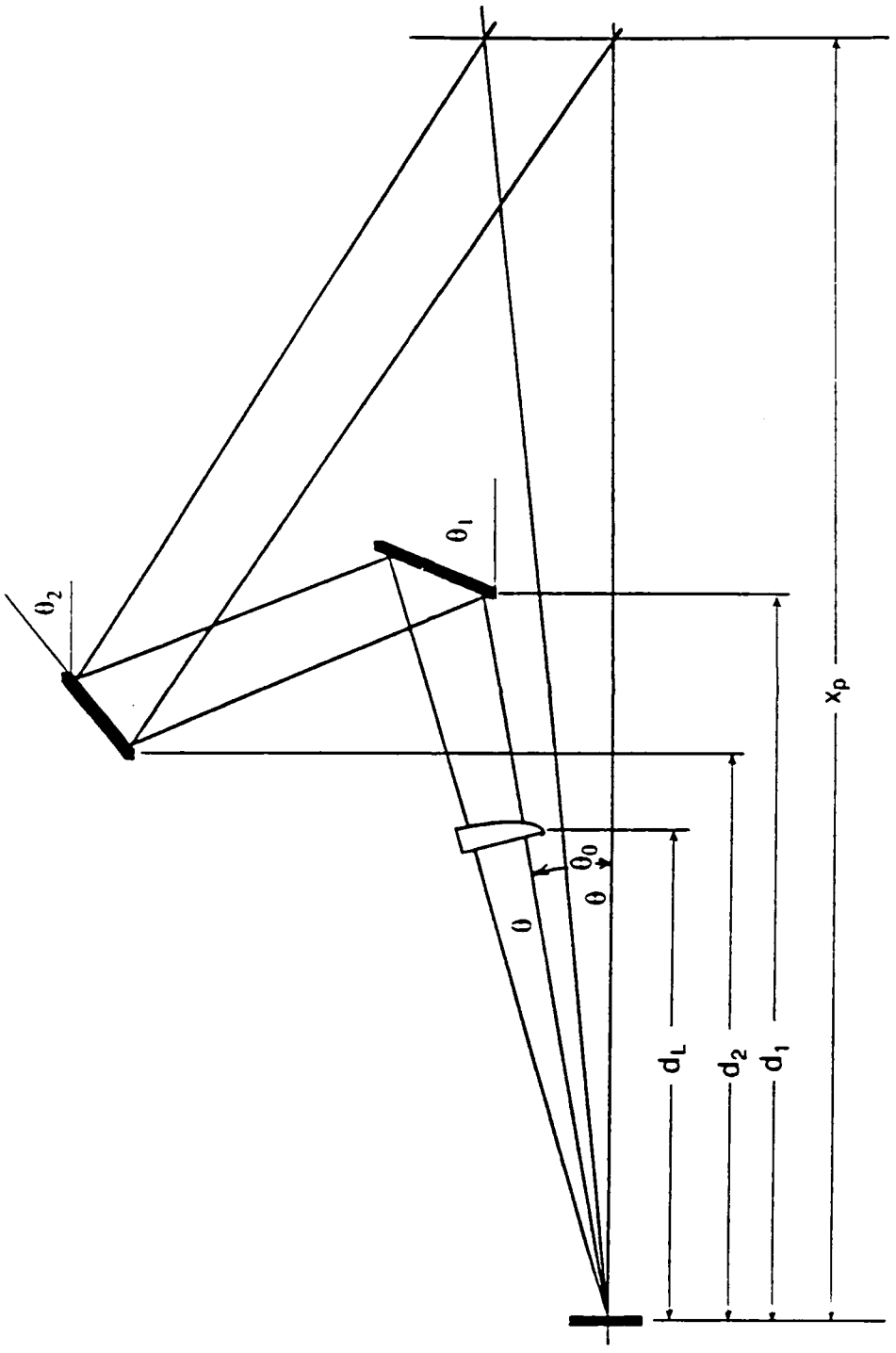

Figure 12. Side View of Vertical Plane Optics: Lens, Plane Mirror Pair.

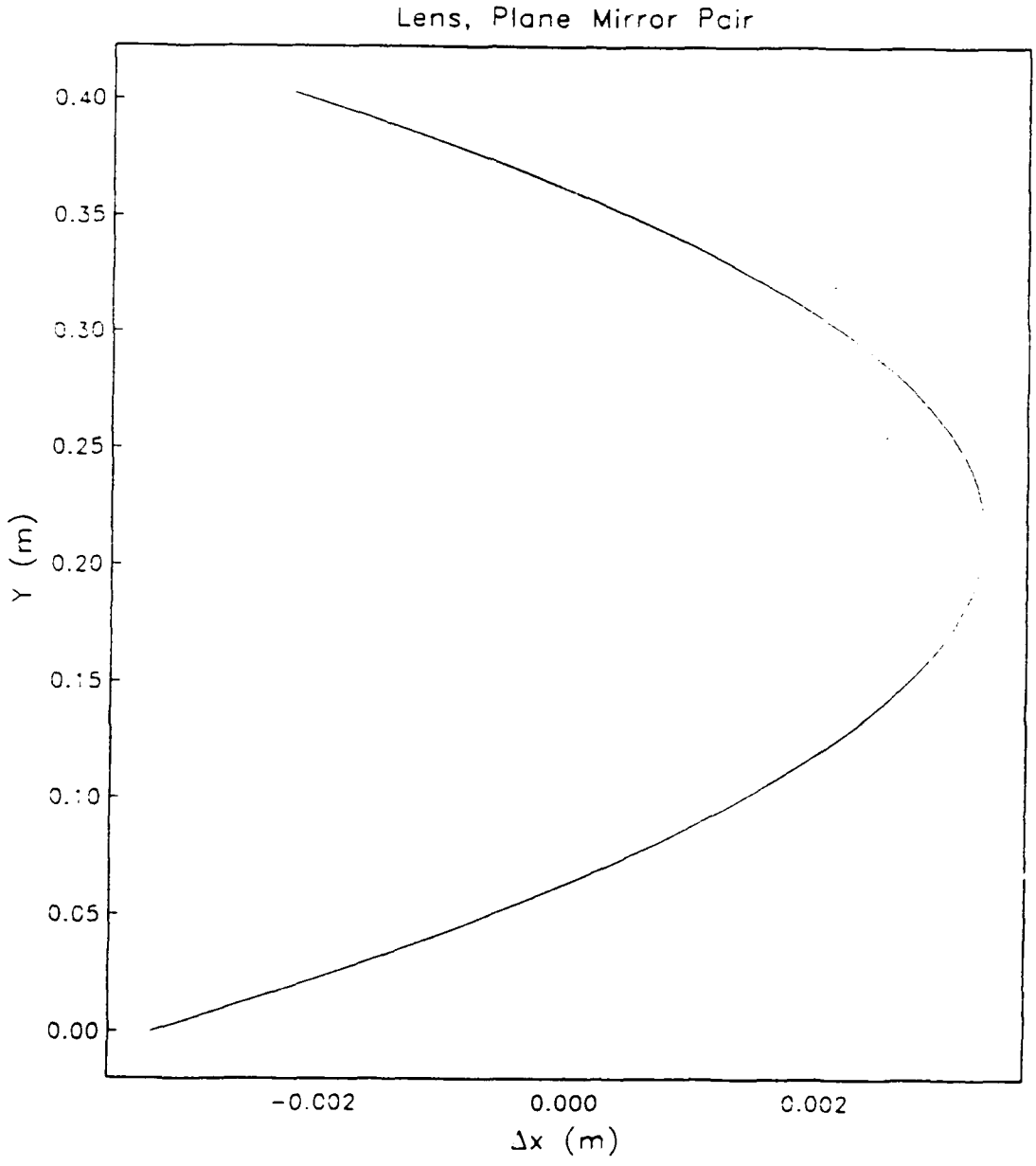

Figure 13. Scan Path of Probe Volumes: Lens, Plane Mirror Pair.

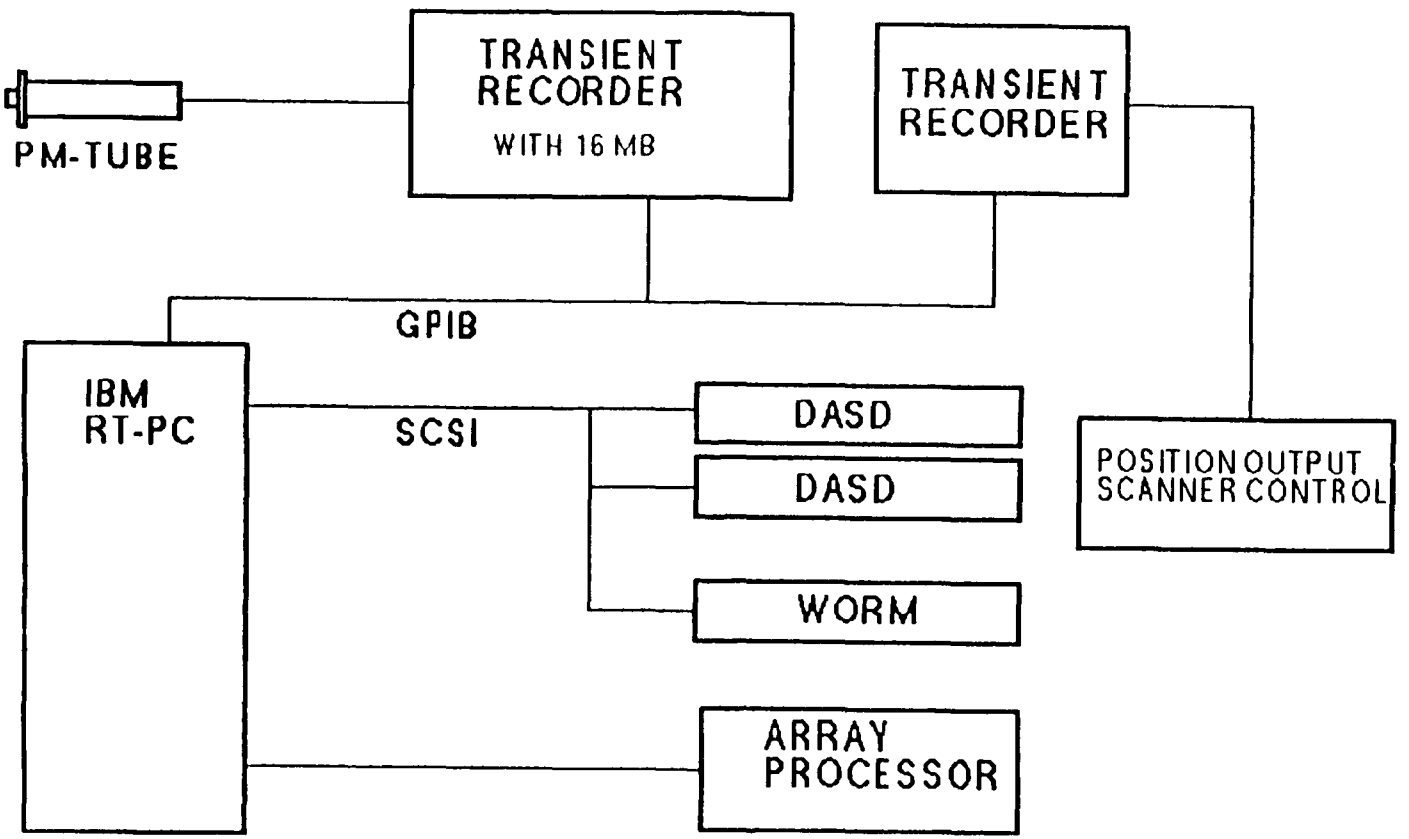

Figure 14. Schematic Diagram of Data Acquistion, Control and Processing System.

APPENDIX A

FIFTH INTERNATIONAL SYMPOSIUM ON
APPLICATION OF LASER TECHNIQUES TO FLUID MECHANICS
AND
WORKSHOP ON THE USE OF COMPUTERS IN FLOW MEASUREMENTS

July 9th-12th, 1990
Lisbon, Portugal

Signal Processing Techniques for Low Signal-to-Noise Ratio Laser Doppler Velocimetry Signals

K. A. Shinpaugh†, R. L. Simpson†, A. L. Wicks‡, and J. L. Fleming†
†Department of Aerospace and Ocean Engineering
‡Department of Mechanical Engineering
Virginia Polytechnic Institute and State University
Blacksburg, VA 24061

ABSTRACT

A variety of methods have been developed to obtain accurate frequency estimates from laser Doppler velocimetry signals. Rapid scanning and fiber optic LDV systems require methods for extracting accurate frequency estimates with computational efficiency from data with poor signal-to-noise ratios. These methods typically fall into two general categories, time domain parametric techniques and frequency domain techniques. The frequency domain approach is initiated by transforming the Doppler bursts in the frequency domain using the fast Fourier transform (FFT). From this basic transformation a variety of procedures have been developed to optimize the frequency estimation accuracy. The time domain approaches are derived from the parametric form of a sinusoid. The estimation of constants in this relationship is performed to satisfy specific constraints, typically a minimization of a variance expression. A comparison of these techniques is presented using simulated signals and additive white noise. The statistical bias and random errors for each method are presented from 200 signal simulations at each condition. Frequency estimation via the FFT was found to be superior to the time domain techniques studied.

NOMENCLATURE

$A(z)$	eigenfilter or characteristic polynomial
a_{M+1}	eigenvector
ACS	autocorrelation sequence
f	frequency, Hz
$\bar{f}$	normalized frequency $\bar{f} = f/f_s$
$\hat{f}_d$	Doppler frequency estimate
f_i	frequency of FFT spectral bin
f_s	sampling frequency
FFT	fast Fourier transform
J	exchange matrix
N	number of sample points in data set
P_i	ith power spectral line from PSD
PHD	Pisarenko harmonic decomposition
PSD	power spectrum density
$r_{xx}(i)$	autocorrelation coefficient for time lag i
R_{M+1}	autocorrelation matrix of order M + 1
RMS	root-mean-square
SNR	signal-to-noise ratio
T	sampling period
$\hat{T}_d$	modified data matrix
Δf	spectral resolution for FFT, $\Delta f = 1/N\Delta t$
Δt	sampling interval

INTRODUCTION

The increased complexity of measured flowfields, the higher degrees of required statistical information, and the development of more sophisticated laser Doppler velocimetry systems (such as rapidly scanning LDV systems) require the processing of low signal-to-noise ratio (SNR) signals to obtain the necessary information. Figure 1 shows a simulated LDV burst at various SNR levels. We would like to be able to obtain accurate Doppler frequency estimates for real signals with SNR below 20 dB down to -10 dB. Traditional LDV signal processors, such as counters, have proven to be both versatile and accurate if the signal-to-noise ratio is high, usually well above 20 dB. In order to obtain accurate frequency estimates at low SNR, frequency domain (non-parametric) or time domain parametric modeling processing must be used.

Processing in the frequency domain offers considerable appeal to the experimentalist from the stand point of speed of computation and familiarity. The fast Fourier transform (FFT) algorithm has been effectively applied for the past 25 years to general signal processing and has become a fixture in the processing of LDV data. The FFT calculates a harmonically related set of sinusoidal components equal to the number of data points in the data set, each with a single degree of freedom. Ensemble-averaging reduces the uncertainty of the spectral estimates; this is typically not available or desirable. To improve the frequency resolution of the FFT, usually some type of interpolation scheme is used.

In time domain parametric methods, an *a priori* assumption of the deterministic content of the signal is made. The nature of the content is assessed based on analysis or knowledge of the process producing the signal, thereby increasing the available statistical degrees of freedom. Parametric techniques make up two classes: autoregressive (AR) based methods and direct parameter estimation techniques. Autoregressive methods work best with wideband signals in noise and tend to produce better spectral shapes but are not as good at locating spectral peaks as compared to direct parameter estimation methods. Direct parameter estimation methods work best for narrowband signals in noise (Marple 1987). LDV signals fall into this classification.

The fast Fourier transform (FFT) algorithm with various interpolation schemes, the Pisarenko harmonic decomposition (PHD) algorithm, and the Eigenvector (EV) algorithm are investigated for processing low SNR LDV signals. The FFT is studied here since it is a widely used technique for processing LDV signals. We would like to know its limits and capabilities in more detail and study the performance of the various interpolation schemes. Also, the FFT can be used as a basis to compare other signal processing techniques. The PHD is computationally faster than the FFT and theoretically has the "ultimate resolution" for sinusoids in white noise (Kay & Marple 1981), which makes it an attractive method for LDV signal processing. The Eigenvector (EV) method is a relatively new technique for frequency estimation which obtains high resolution of narrowband signals in noise, even with small data sets (Marple 1987).

Each algorithm was evaluated with respect to bias (mean) frequency error, root-mean-square (RMS) frequency error, and computation time as a function of frequency (fraction of sampling frequency), number of sample points, and signal-to-noise ratio (SNR). Testing was performed with computer simulated Doppler signals with specified frequency (fraction of sampling frequency), number of data points, and SNR. These signals were generated by adding white noise with Gaussian distributed amplitude to a Gaussian weighted sinusoid to obtain a simulated signal with the

desired parameters (see Figure 1). Statistical information presented (bias error and RMS error) is based on 200 realizations. For each realization, a statistically independent white noise sequence was added to the simulated Doppler burst. For the evaluation of the SNR, the variance of the white noise was fixed to generate the specific SNR. The signal-to-noise ratio is given by

$$SNR = 10\log_{10}\left[\frac{\text{mean square of signal}}{\text{variance of noise}}\right] \quad (1)$$

In this paper all frequencies have been normalized by the sampling frequency, and all frequency errors are given as percentage of the sampling frequency.

FAST FOURIER TRANSFORM

The fast Fourier transform is employed in Doppler frequency estimation by calculating the power spectral density (PSD) of a Doppler burst. In the frequency domain as displayed in the PSD, the desired signal is easily separated from the noise. The resolution obtained from the PSD is inversely proportional to the total sample period; N spectral lines are obtained for N input data points spanning the frequency domain of -0.5 to 0.5 of the sampling frequency. A common technique to improve the estimate of the Doppler frequency of an LDV burst is to fit a parabola through the spectral peak and several adjacent spectral lines (Kalb & Crosswy 1983). The motivation for using a parabola is that it is a symmetric function and simple to evaluate, but it can also be shown to be the logical function to use. The Fourier transform of a Gaussian function or window is also a Gaussian function or window. Thus, the Fourier transform of a Gaussian LDV burst results in a Gaussian function centered at the Doppler frequency. Taking the natural logarithm of the spectrum results in a parabola centered at the Doppler frequency. Another interpolation technique is to fit a Gaussian curve to the spectral lines (Hishida *et al.* 1989).

The application of time domain weighting functions (windows) to LDV data blocks have been discussed by several authors (Bachalo *et al.* 1989, Matovic & Tropea 1990). The application of specific windows to sinusoidal content is defined by the convolution of the frequency domain representation of the sinusoid. Symmetric windows such as the Hanning window (*Hann*), when applied to white noise data, reduce the variance of the spectrum and thus has been promoted as an asset (Harris 1978). Since the signal content of LDV data has a Gaussian amplitude weighting already, the application of additional windows to the data complicates the convolution of the signal content while reducing the variance of the noise content. As a result, this study was performed independent of windows in addition to the Gaussian.

The estimate for the Doppler frequency is found from the zero-slope intercept of a parabolic regression applied (Eq. 2) to the largest and two adjacent spectral lines. The parabolic fit applied to an LDV burst is illustrated in Figure 2.

$$\hat{f}_d = f_i + \left[\frac{P_{i-1} - P_{i+1}}{2[P_{i-1} + P_{i+1} - 2P_i]}\right]\Delta f \quad (2)$$

The Gaussian fit is applied in a similiar manner and is given by (Eq. 2) (Hishida *et al.* 1989)

$$\hat{f}_d = f_i + \left[\frac{\ln(\frac{P_{i-1}}{P_i}) - \ln(\frac{P_{i+1}}{P_i})}{2[\ln(\frac{P_{i-1}}{P_i}) + \ln(\frac{P_{i+1}}{P_i})]}\right]\Delta f \quad (3)$$

A log parabolic fit can be made by taking the natural logrithm of the spectral lines in Eq. (2); this is equivalent to Eq. (3). This method is unstable for SNR levels below 0 dB. Zero-padding is also another technique used to enhance the accuracy of estimating the frequency of spectral peaks (Kay & Marple 1981) and can be used in conjunction with any of the above interpolation methods. For the cases studied here, only N set of zeros was added to the data set to give a total record length of 2N.

Some results for the fast Fourier transform with various interpolation schemes applied to simulated LDV signals are shown in Figures 3-8. Figures 3 and 4 show the RMS frequency error as a function of SNR and the number of sample points, N, at a normalized (by sampling frequency) frequency of $f = 0.225$ for the parabolic fit and Gaussian fit with and without zero-padding. The frequency $f = 0.225$ does not fall on any spectral line for the number of points, N, studied and was selected for this reason. As expected, a doubling in the number of sample points results in a factor of approximately 2 reduction in the RMS error for each technique. Also, the methods show a region where the RMS error is relatively constant with SNR; in this region the noise power does not significantly impact the power content in each spectral line. At some point the RMS error gradually increases with decreasing SNR until some limiting value of SNR is reached where the RMS frequency error increases rapidly. This is due to the noise contributing more and more power to each spectral line, until even in the frequency domain the signal is buried in noise. This effect is more pronounced for the cases with fewer sample points. Since the power due to noise is distributed approximately equally between the spectral lines and the power content in the signal is only contained in a few spectral lines, as the number of spectral lines decreases, the energy content of each spectral line due to noise increases, but the energy content due to the signal remains constant. The Gaussian interpolation provides about a factor of 3 decrease in the RMS frequency error over the parabolic fit at high SNR but, at low SNR the methods are equal. Zero-padding improves the RMS error by an order of magnitude at high SNR, but is the same at the SNR limit. Note that zero-padding does not change the SNR limit; thus, the underlying resolution of the FFT is not increased by this method.

Figures 5 and 6 show the RMS frequency error normalized by the FFT resolution Δf as function of signal frequency relative to a PSD spectral line or FFT bin (round $[fN]$). The cases shown are for N = 128 points and SNR's of 50 dB and 0 dB. Since the RMS error is normalized by Δf the variation based on the number of data points is negligible, except when the SNR limit has been reached for that particular N. Note that in both cases the RMS error is symmetric about a spectral line. For the case of $SNR = 50$ dB, when the signal lies at ± 0.5 and 0 for methods without zero-padding and ± 0.5, ± 0.25 and 0 for mehtods using zero-padding, the RMS error is nearly zero, below 10^{-3}. As the SNR decreases, the RMS error becomes less dependent on relative frequency and eventually is flat across the domain, except for the parabolic fit without zero-padding. These results agree with those obtained by Hishida *et al.* (1989) for the Gaussian fit without zero-padding.

Figures 7 and 8 show the frequency bias error normalized by the FFT resolution Δf as a function of the signal frequency relative to a PSD spectral line or FFT bin. Again, since the mean or bias error has been normalized by Δf, there will be negligible dependence on the number of data point N above the SNR limit. The bias error is antisymmetric about zero relative frequency. The parabolic fit appears to be biased toward the closest spectral line and the Gaussian fit to the next closest spectral line. The bias error is nearly zero for relative frequencies of ± 0.5 and 0 for methods without zero-padding and ± 0.5, ± 0.25 and 0 for methods with zero-padding. The bias error does not change much with SNR, except when the SNR limit has been reached where the bias error increases rapidly (Shinpaugh 1989). These results agree with those obtained by Bachalo *et al.* (1989) for the parabolic and Gaussian fit without zero-padding.

The computation time is constant with SNR for each case, and there is no difference between using the parabolic fit or Gaussian fit as far as computation time is concerned. The use of zero-padding approximately doubles the computational time over the FFT algorithms without zero-padding (Shinpaugh 1989).

PISARENKO HARMONIC DECOMPOSITION

The Pisarenko harmonic decompostion (PHD) is a parametric estimation method that assumes that the process consists of sinusoids in additive white noise (Pisarenko, 1973). The sinusoidal frequencies and white noise power are obtained from an eigenvalue analysis of the time-delay autocorrelation matrix. The noise power is equal to the minimum eigenvalue of the autocorrelation matrix of appropriate order and the sinusoidal frequencies are computed from the roots of the characteristic polynomial (eigenfilter) associated with the minimum eigenvalue (Hayes & Clements 1986).

The autocorrelation sequence (ACS) contains information concerning the power and frequency of each sinusoid. Note that the white noise exists only in the zeroth lag. The autocorrelation matrix R_{M+1} formed from the ACS will have the form

$$R_{M+1} = \begin{bmatrix} r_{xx}(0) & \cdots & r_{xx}(M) \\ \vdots & \vdots & \vdots \\ r_{xx}(M) & \cdots & r_{xx}(0) \end{bmatrix} \quad (4)$$

The minimum eigenvalue of R_{M+1} and associated eigenvector a_{M+1} correspond to the white noise variance and the reflection coefficients, respectively. The eigenvector a_{M+1} associated with the minimum eigenvalue forms the characteristic equation

$$A(z) = \sum_{k=0}^{M} a_{M+1}(k+1)z^{-k} \tag{5}$$

where $A(z)$ is also known as the eigenfilter of $w(n)$. The roots of the eigenfilter will lie on the unit circle at angles $2\pi f_i T$ for $1 \le i \le M$, and hence determine the sinusoidal frequencies. For M real sinusoids in white noise, the ACS must be known for lags of 0 to 2M; 2M roots will be obtained from the eigenfilter (Marple 1987).

Some of the results for the PHD algorithm are shown in Figures 9-11. Figure 9 shows the RMS frequency error as a function of SNR and number of sample points. The RMS error is extremely low for high SNR but increases almost linearly at a rate of a magnitude per decade decrease in SNR. The bias error is approximately zero for SNR above 5 dB, and increases as the SNR falls below this point, as shown in figure 10. Also, the number of sample points does not appear to be a major factor in the bias error. The RMS frequency error as a function of normalized frequency and number of sample points for the PHD algorithm for the case of SNR = 50 dB is shown in Figure 11. The RMS error is lowest for frequencies near half the Nyquist frequency and increases for frequencies near zero and the Nyquist. The RMS error is also symmetric about the half Nyquist frequency. At other SNR levels the shape of RMS error as a function of f is approximately the same (Shinpaugh 1989). Aktar *et al.* (1985) obtained similar results for pure sinusoids in white noise by theoretical analysis and simulation.

EIGENVECTOR ALGORITHM

The Eigenvector method (EV) is similar to the PHD algorithm in that an eigenanalysis is applied to an autocorrelation like matrix. Consider, for example, a signal containing a single sinusoidal component with additive noise. The signal vector space would therefore span a 2M dimensional subspace where M represents the number of sinusoidal signals. The autocorrelation-like matrix is of rank p where p> 2M thus p-2M determines the noise subspace. The 2M principal eigenvectors of the data matrix predominantly span the signal subspace, and the singular values (eigenvalues) of these principal eigenvectors tend to be larger than the noise subspace singular values. This allows the separation of the eigenvalues into mostly signal subspace and a mostly noise subspace, effectively enhancing the SNR. Functions of the vectors in either the signal or noise subspace can be used to provide frequency estimates (Marple 1987).

The Eigenvector method performs an eigenanalysis on a modified data matrix in the form of

$$\hat{T}_p = \begin{bmatrix} T_p \\ T_p J \end{bmatrix} \tag{6}$$

where

$$J = \begin{bmatrix} 0 \dots 0 & 1 \\ 0 \dots 1 & 0 \\ \vdots & \vdots \\ 1 & 0 \dots 0 \end{bmatrix}$$

and

$$T_p = \begin{bmatrix} x_{p-1} \dots x_1 \\ \vdots \\ x_N \dots x_{N-p} \end{bmatrix}$$

For the noise-free complex exponential sequence

$$x = \sum_{k=1}^{M} h_k z_k^n \tag{7}$$

where

$$h_k = A_k \exp j\phi_k$$

$$z_k = \exp[\alpha_k + j2\pi f_k]T$$

The modified data matrix, $\hat{T}_p$, formed from x will have rank M and M nonzero eigenvalues. A singular value decomposition is performed on the autocorrelation like matrix, $T_p^* T_p$, and results in the following

$$T_p^* T_p v_i = \lambda_i v_i \tag{8}$$

for $1 \le i \le M$. The remaining $p - M$ eigenvalues are zero. The principal eigenvectors of $T_p^* T_p$ are a linear combination of the columns of a matrix composed of signal vectors. The eigenvectors corresponding to the zero eigenvalues are orthogonal to the M signal subspace eigenvectors.

In the presence of noise, the properties of the data matrix are not quite the same. The principal eigenvalues associated with the signal subspace are typically larger than the $p - M$ noise subspace eigenvalues and therefore can be separated. The eigenvectors associated with the noise subspace are theoretically orthogonal to the sinusoidal signal vectors. Therefore, the inner product with arbitary weighting will be zero when a noise vector corresponds to a sinusoid vector. Inverting the inner product drives the coincidence of the noise vectors and signal vectors to infinity, thus allowing the identification of the frequency content. For a more detailed description of this algorithm, see Marple (1987).

Some results for the EV method are shown in Figures 12-15. Due to the complexity of this method, the number of sample points had to be limited to below 512 points. The RMS frequency error as a function of SNR and the number of sample points, N, for a normalized frequency of $f = 0.225$ is shown in Figure 12. The RMS error is fairly constant to about 20 dB and then rises at an order of magnitude per decade. The apparent better performance of the method with N = 64 points is probably due to the effects of sampling density. The bias error as a function of SNR and N is shown in Figure 13. the bias error is fairly constant down to about 10 dB SNR but increases rapidly below -10 dB SNR. The bias error is not identically zero because of the use of a FFT to produce a spectrum and the subsequent application of a parabolic fit to determine the frequency. The effects of normalized frequency on the RMS error is shown in Figure 14 for an SNR of 50 dB. As can be seen from this plot, the RMS error is symmetric about $f = 0.25$, and the sampling density has a great effect on the RMS error. The EV method behaves in a similiar manner to the PHD algorithm, which is not surprising since both use an eigenanalysis on an autocorrelation-like matrix.

CONCLUSIONS

The RMS frequency error and the bias frequency error for the FFT methods do not depend on f except on where f falls relative to a PSD spectral line. Also, the RMS frequency error becomes independent of f when the SNR is below 10 dB. With either the parabolic or Gaussian interpolation schemes, the zero-padding procedure for the FFT reduces the RMS frequency error to a few percent at low SNR and an order of magnitude lower at high SNR compared to the same interpolation scheme without zero-padding. Also, zero-padding reduces the bias error typically an order of magnitude. However, zero-padding increases the computation time by a factor of approximately two. The Gaussian interpolation method for the FFT provides a factor of 3 improvement in the RMS and bias error at SNR levels above 0 dB compared to the FFT with the parabolic fit. The Gaussian interpolation method with zero-padding gives the highest resolution for signals with an SNR above -6 dB. Below this point, zero-padding does not improve the results, so the Gaussian fit without zero-padding is to be used.

The PHD algorithm is typically an order of magnitude faster computationally compared to the FFT algorithms. The bias error for the PHD at higher SNR levels is smaller than the bias errors obtained for the FFT algorithms without zero-padding for frequencies away from zero and the Nyquist frequency. Only at high SNR levels, above 30 dB, and only at certain frequencies does the PHD algorithm outperform the FFT algorithms with respect to the level of RMS error. The EV method does not compare well to either the FFT or PHD algorithms except maybe where the number of sample points are very few, below N = 32. This can be seen in Figure 15, which shows the domain or region at which each algorithm is the most effective. As an example, if the SNR levels from the photomultiplier tube (after filtering) were at 20 dB then the FFT with zero-padding and log parabolic interpolation would provide the most accurate frequency estimates. As can be seen from Figure 15, the switch points between the two FFT algorithms occurs at the same SNR level regardless of the frequency. However, the dividing line between when to use the PHD algorithm and the FFT with zero-padding and Gaussian interpolation algorithm is dependent on the frequency and the number of samples in the data record. From this map it is possible to tell which algorithm to use if an approximate SNR and frequency is known for the signal to

be processed.

References

Akter, M., Sankur, B., and Istefanopulos, Y. 1985 "Properties of the Maximum Likelihood and Pisarenko Spectral Estimates" *Signal Processing, vol. 8*, pp 401-413.

Buchalo, W.D., Werthimer, D., Raffanti, R., and Hermes, R.J. 1989 "A High Speed Doppler Signal Processor for Frequency and Phase Measurements" *Third Int. Conf. on Laser Anemometry - Advances and Applications*, Swansea.

Harris, F.J. 1978 "On the use of Windows for Harmonic Analysis with the Discrete Fourier Transdorm" *Proc. of the IEEE* vol. 66, No. 1, pp 51-83.

Hayes, M.H., and Clements, M.A. 1986 "An Efficient Algorithm for Computing Pisarenko's Harmonic Decomposition Using Levinson's Recursion", *IEEE Trans. ASSP, ASSP-34, no. 3*, pp 485-491.

Hishida, K., Kobashi, K., Maeda, M. 1989 "Improvement of LDA PDA Using A Digital Signal Processor (DSP)" *Third Int. Conf. on Laser Anemometry - Advances and Applications*, John T Turner, ed., Univ. of Manchester, Swansea, paper S.2.

Kalb, H.T., and Crosswy, F.L. 1983 "Discrete Fourier Transform Signal Processor for Laser-Doppler Anemometry" *AEDC-TR-83-46*, Arnold Engineering Development Center AAFS, Tennessee.

Kay, S.M., and Marple, S.L. 1981 "Spectrum Analysis - A Modern Perspective" *Proc. IEEE*, vol. 69, pp 1380-1419.

Marple, S.L., Jr. 1987 *Digital Spectral Analysis with Applications*, Prentice Hall, New Jersey.

Matovic, D., Tropea, C., and Martinuzzi, R. 1987 "Frequency Estimation of LDA Signals by Model Parametric Estimation" *The Use of Computers in Laser Velocimetry, Inst. St. Louis Report R/05/87*, H.J. Pfeifer and B. Jaeggy, editors.

Pisarenko, V.F. 1973 "The Retrieval of Harmonics from a Covariance Function" *Geophys. J. Roy. Astron. Soc.*, vol. 33, pp 347-366.

Shinpaugh, K.A. 1989 "Design of a Rapidly Scanning 3-D Laser Doppler Velocimeter with Low SNR Signal Processing" *MS Thesis, Dept. Aero. Engr., VPI&SU.*

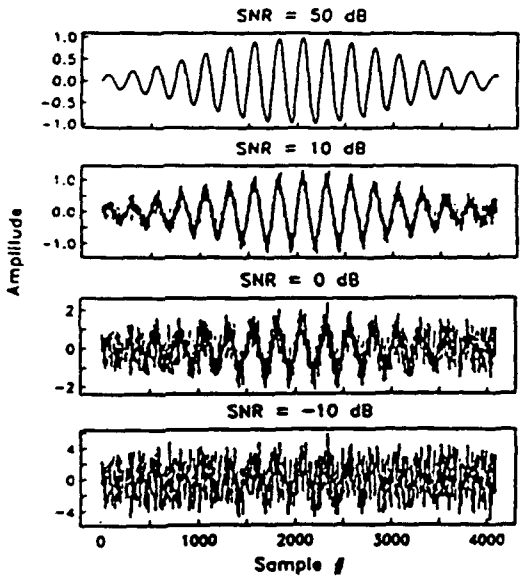

Figure 1. Simulated LDV burst signals at various SNR levels.

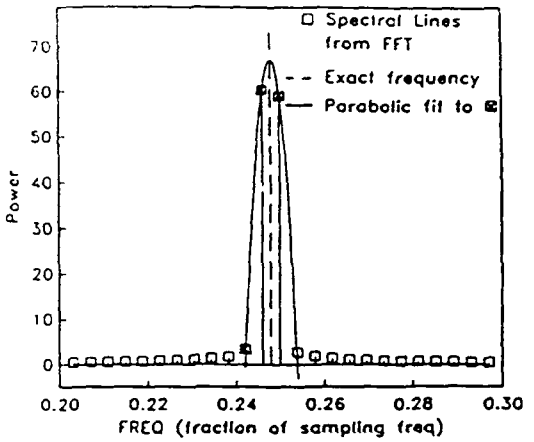

Figure 2. Illustration of the parabolic fit to a burst PSD.

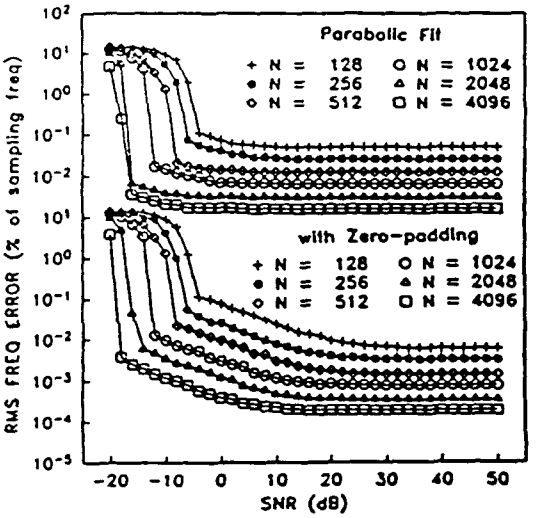

Figure 3. RMS frequency error vs. SNR for the parabolic fit with and without zero-padding at $\tilde{f}$ = 0.225.

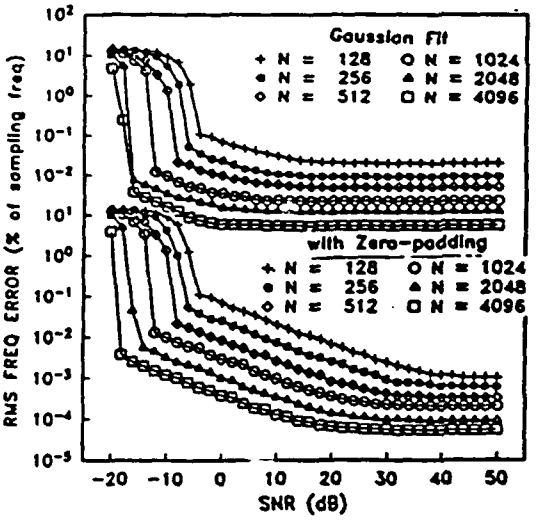

Figure 4. RMS frequency error vs. SNR for the Gaussian fit with and without zero-padding at $\tilde{f}$ = 0.225.

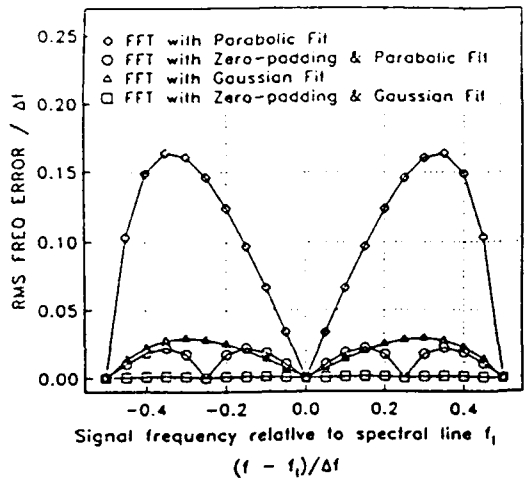

Figure 5. RMS frequency error normalized by FFT spectral resolution as a function of the signal frequency relative to a spectral line for the FFT methods, SNR = 50 dB.

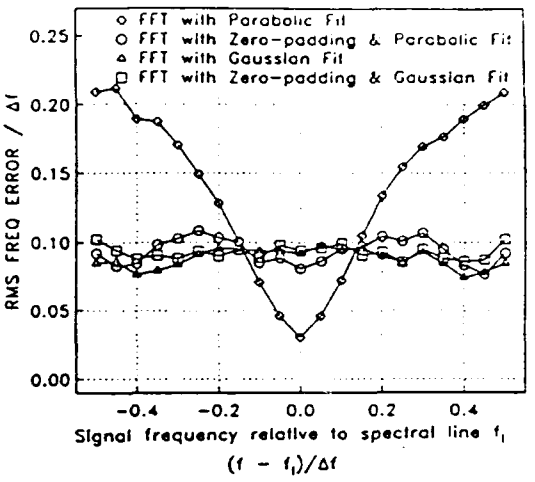

Figure 6. RMS frequency error normalized by FFT spectral resolution as a function of the signal frequency relative to a spectral line for the FFT methods, SNR = 0 dB.

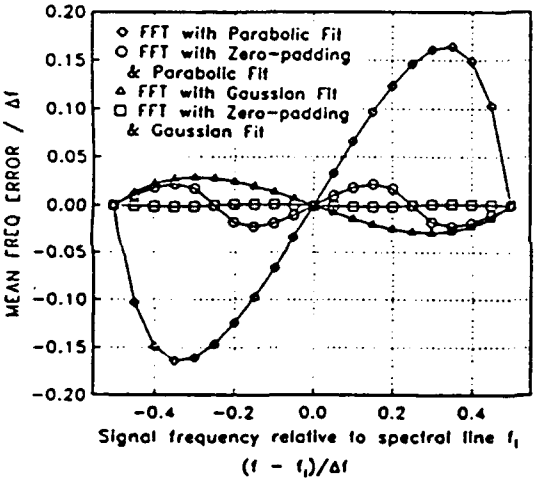

Figure 7. Frequency bias error normalized by FFT spectral resolution as a function of the signal frequency relative to a spectral line for the FFT methods, SNR = 50 dB.

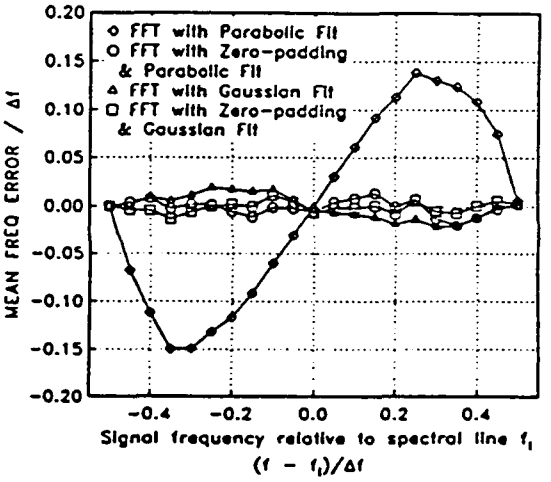

Figure 8. Frequency bias error normalized by FFT spectral resolution as a function of the signal frequency relative to a spectral line for the FFT methods, SNR = 0 dB.

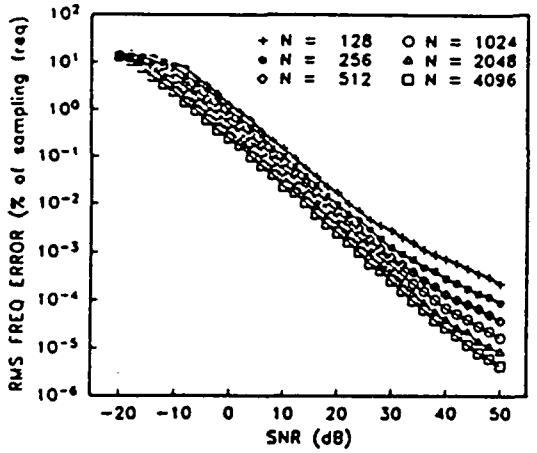

Figure 9. RMS frequency error vs. SNR for PHD at $\bar{f} = 0.25$.

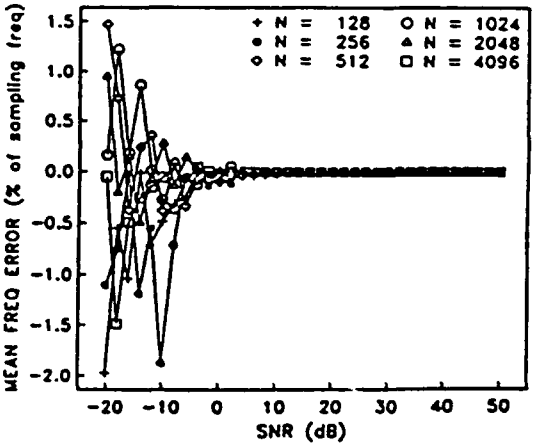

Figure 10. Frequency bias error vs SNR for PHD at $\bar{f} = 0.25$.

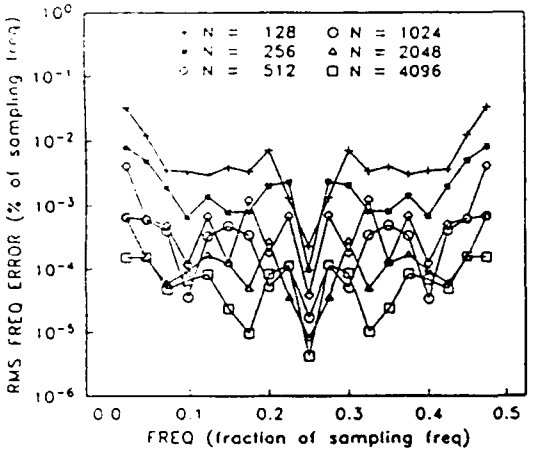

Figure 11. RMS frequency error vs. frequency for PHD at SNR = 50 dB.

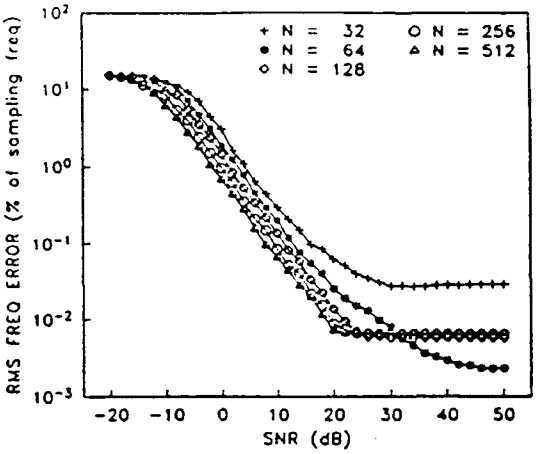

Figure 12. RMS frequency error vs SNR for EV at $\bar{f}$ = 0.225.

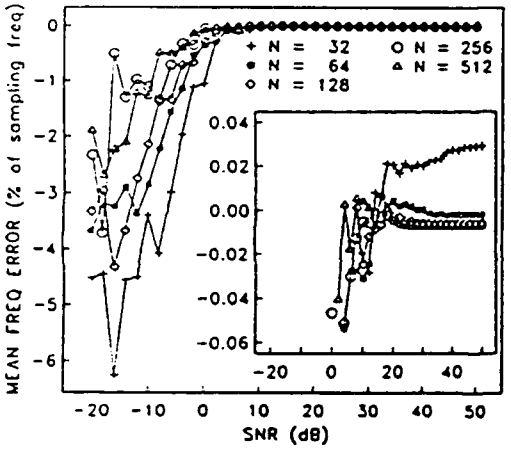

Figure 13. Frequency bias error vs SNR for EV at $\bar{f}$ = 0.225.

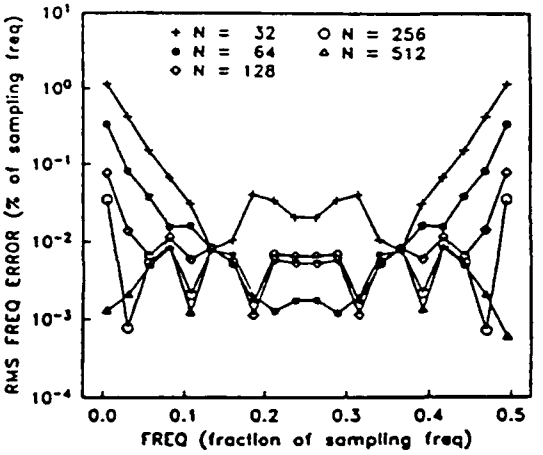

Figure 14. RMS frequency error vs frequency for EV at SNR = 50 dB.

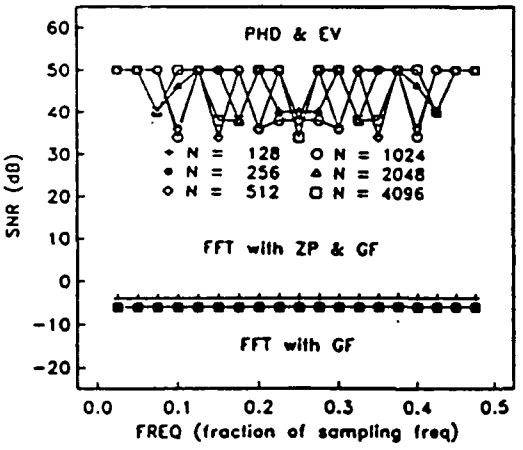

Figure 15. SNR vs frequency identifying the appropriate technique to use relative to SNR and frequency. : GF = Gaussian fit, ZP = zero-padding.